
Ab Initio Green-Kubo Calculations for Strongly Anharmonic Solids: A comparative Benchmark of Lattice Thermal Conductivities

Master thesis by Xiaoyu Zhu

Date of submission: June 27, 2022

1. Review: Prof. Karsten Albe
2. Review: Dr. Christian Carbogno
Darmstadt



TECHNISCHE
UNIVERSITÄT
DARMSTADT

Department of Materials
and Geosciences
Institute of Materials
Science

Erklärung zur Abschlussarbeit gemäß §22 Abs. 7 und §23 Abs. 7 APB der TU Darmstadt

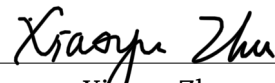
Hiermit versichere ich, Xiaoyu Zhu, die vorliegende Masterarbeit ohne Hilfe Dritter und nur mit den angegebenen Quellen und Hilfsmitteln angefertigt zu haben. Alle Stellen, die Quellen entnommen wurden, sind als solche kenntlich gemacht worden. Diese Arbeit hat in gleicher oder ähnlicher Form noch keiner Prüfungsbehörde vorgelegen.

Mir ist bekannt, dass im Fall eines Plagiats (§38 Abs. 2 APB) ein Täuschungsversuch vorliegt, der dazu führt, dass die Arbeit mit 5,0 bewertet und damit ein Prüfungsversuch verbraucht wird. Abschlussarbeiten dürfen nur einmal wiederholt werden.

Bei der abgegebenen Thesis stimmen die schriftliche und die zur Archivierung eingereichte elektronische Fassung gemäß §23 Abs. 7 APB überein.

Bei einer Thesis des Fachbereichs Architektur entspricht die eingereichte elektronische Fassung dem vorgestellten Modell und den vorgelegten Plänen.

Darmstadt, 27. Juni 2022


Xiaoyu Zhu

Contents

1. Introduction/Motivation	6
2. Fundamental Principles	11
2.1. Solution to Schrödinger Equation	11
2.1.1. Hartree-Fock Approximation	12
2.2. Density Functional Theory	13
2.2.1. Hohenberg-Kohn theorems	13
2.2.2. Kohn-Sham Method	14
2.2.3. Exchange-Correlation Functional	16
2.2.4. Solution to Kohn Sham Equations	18
2.3. Dynamic lattice model	19
2.3.1. Harmonic approximation	19
2.3.2. Beyond Harmonic approximation	21
2.3.3. Phonon interaction and thermal conductivity	25
2.4. Molecular dynamics	28
2.4.1. Verlet algorithms	30
2.4.2. Ensembles	31
2.4.3. Langevin thermostat	32
2.4.4. Anharmonicity	36
2.5. The Green-Kubo calculation method	39
2.5.1. Linear response theory	39
2.5.2. Equilibrium time correlation functions	42
2.5.3. Heat flux autocorrelation function	43
2.5.4. Heat flux	44
2.5.5. Thermal conductivity via <i>ab initio</i> Green-Kubo calculation	47
3. Toy model calculation	49
3.1. Relaxation	50

3.2. Phonon calculation	51
3.2.1. Thermal conductivity by lattice dynamics method	54
3.3. Molecular dynamic calculation	55
3.3.1. Anharmonicity quantification	57
3.4. Heat conductivity	59
3.4.1. Heat flux autocorrelation function	59
3.4.2. Thermal conductivity by Green-Kubo method	61
4. Properties of Magnesium oxide	63
4.1. Vibrational Properties of MgO in the Harmonic Approximation	64
4.2. Lattice thermal conductivity by phono3py calculation	66
5. Thermal Conductivities for Strongly Anharmonic Compounds	71
6. Conclusion	78
Appendices	87
A. Thermal conductivity for MgO with different supercell size	87
B. Vibrational properties of Strongly Anharmonic CsF	91
C. Vibrational properties of Strongly Anharmonic LiGaTe	94
D. Vibrational properties of Strongly Anharmonic Lil	95
E. Vibrational properties of Strongly Anharmonic KCaF	98

Abstract

Understanding heat transport in semiconductors and insulators is of fundamental significance, for instance, for renewable energy harvesting and conversion in thermoelectric devices. Lattice dynamics provides a powerful framework for the description of heat transport from the phonon scattering perspective and naturally includes quantum effects in the atomic vibrations. However, only the leading orders of anharmonicity are accounted for. In comparison, the Green-Kubo method is based on equilibrium Molecular dynamics simulations and the fluctuation-dissipation theorem is utilized to calculate the thermal conductivity for materials with strong anharmonicity. In this method, anharmonic effects are fully accounted for, but quantum-mechanical effects are not included in the nuclear dynamics. A comparison between these two methods is needed to understand under which circumstances which method is preferable. Most importantly, this sheds light on the validity range of the respective approximations, i.e., the perturbative treatment of anharmonicity and the classical treatment of the nuclear dynamics.

1. Introduction/Motivation

Thermal conductivity describes the capability of a material to conduct heat. Heat transport describes the flow of the thermal energy or heat flux due to a temperature gradient. The physical mechanism of heat transport can be related to different kinds of heat carriers, namely, electrons, photons or phonons. In metals, electrons and phonons can both transfer heat, while in nonmetals, i.e. semiconductors or insulators, thermal transport is exclusively dominated by phonons especially at high temperature. In this work we focus on the phonon contributions to the thermal conductivity. Heat transport and thermal conductivity play a vital importance in many scientific and engineering applications, for example, earth science[1, 2], building components[3] and electronic devices[4]. Among these diverse applications, thermoelectric materials and devices, based on the direct and reversible energy conversion between heat and electricity, can help addressing the global energy dilemma.[5] To be more specific, in a thermoelectric power generator, the hot ends of the n-type and p-type semiconductor material are electrically connected and a load is connected across the cold ends. Due to the Seebeck effect, voltage is produced and will impose a current to flow through the load, generating electrical power. This process is illustrated on the left side of Fig. (1.1) and a reverse process is shown in the right part.

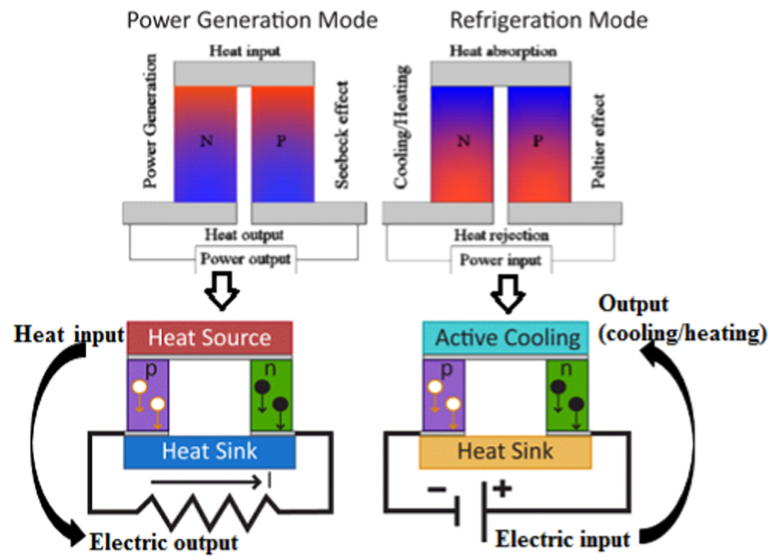


Figure 1.1.: Power generation and cooling/heating thermoelectric heat engines by a solid-state device. Fig from Ref.[6]

The conversion efficiency of a thermoelectric material can be quantified by the dimensionless figure-of-merit

$$ZT = \frac{S^2\sigma}{\kappa}T = \frac{S^2\sigma}{\kappa_e + \kappa_l}T, \quad (1.0.1)$$

with S the Seebeck coefficient, σ the electric conductivity and κ thermal conductivity. The latter consists of both the electron and phonon contributions, denoted as κ_e and κ_l . As Eq. (1.0.1) suggests, the performance of a thermoelectric material can be improved by increasing the power factor $S^2\sigma$, by reducing the lattice thermal conductivity by introducing scattering centers. However, the interdependency of these processes challenges such enhancement efforts. For example, for most of the homogeneous materials, the carrier concentration increases electrical conductivity but reduces the Seebeck coefficient[7]. Based on a kinetic definition, S is the energy difference between the average energy of mobile carriers and the Fermi energy[8], and the Fermi energy increases faster than the average energy when a larger carrier density is given. In this sense, increasing the carrier density leads to smaller Seebeck coefficients. This coupling effect for electron coefficients applies also for the electrical conductivity and the electronic contribution to the thermal

conductivity according to the famous Wiedemann–Franz Law[9]

$$k_e/\sigma = LT. \quad (1.0.2)$$

In contrast to the interdependent electronic coefficients, phonon contributions which will also be the core of this work are mostly independent. Nanoscale constituents are used to introduce quantum confinement effects to increase power factors and provide many internal interfaces to scatter phonons.[7, 10] The change of phonon group velocities and dispersion due to the spatial confinement leads to the increase of the phonon relaxation rate and a considerable drop in lattice thermal conductivity.[7] To be more specific, Bismuth nanotubes and nanowires are shown as an example in Fig. (1.2). Here, the thermal conductivity is suppressed to 5 times less than that of Bismuth powder.

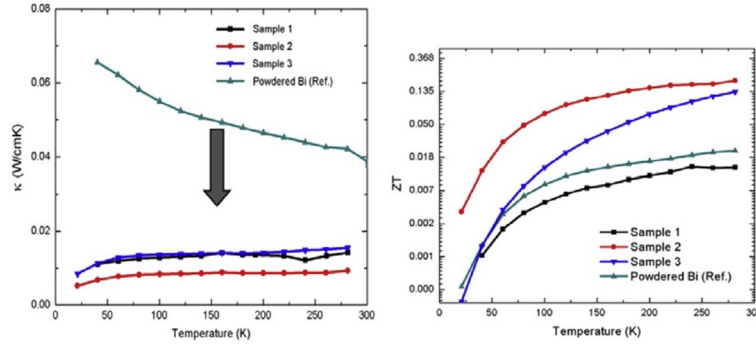


Figure 1.2.: Thermal conductivity and ZT as a function of temperature for three Bi nanostructured network samples in comparison with the Bi reference. Fig from Ref.[11]

Due to the many applications, the theoretical prediction of lattice thermal conductivity is of paramount importance in the studies of thermal transport properties of solid materials, where lattice vibrations contribute mostly.[12] Theoretical studies of thermal conductivity can be divided into two classes, lattice dynamics (LD) and molecular dynamics (MD). The LD method computes the harmonic and anharmonic force constants and solves the phonon *Boltzmann Transport Equation*[13, 14] to obtain the thermal conductivity. This method highly relies on the lattice symmetry to reduce the calculation complexity. Normally, it only considers the three-phonon scattering process to circumvent the high order anharmonic force constant calculations. In comparison to the LD method which focus on the phonons, MD method is a real-space approach which tracks the position and momentum of each atom. In this method, the only required inputs are an initial condition and a model for

predicting the forces between atoms, for instance, an empirical potential, or obtained from density functional theory (DFT) calculations. There are two widely-used MD-based methods for predicting thermal conductivity, direct method based on nonequilibrium MD and Green–Kubo method based on equilibrium MD. In the direct method, a temperature gradient is imposed on the simulation cell and the thermal conductivity is calculated by *Fourier’s law*. [15] Conversely, the Green–Kubo method relates the equilibrium current fluctuations to the thermal conductivity according to the *fluctuation-dissipation theorem*, [16] which requires smaller cells compared to the direct method. The limits of the above-mentioned classical MD lie on the underestimation of nuclear quantum effects (NQEs), such as delocalization, zero-point energy, and tunneling [17], which leads to errors while studying systems with hydrogen bonds or organic molecules featuring a C-H bond. [18]

In this thesis, the applicability and validity of both the lattice method and Green-Kubo method will be inspected and compared for different compounds. The thesis will be organised in a way that the first part introduces the theoretical concepts to understand the thermal conductivity calculation. In sec. (2.1, 2.2) the quantum mechanical many-body problem and Density Function Theory (DFT) as an approximation method for solving the electronic problem are introduced. Section (2.3) presents nuclear dynamics model by taking harmonic approximation as a powerful starting point and goes beyond to anharmonicity, which plays a vital role in thermal conductivity calculation. Section (2.4) is dedicated to the key concepts of Molecular dynamics simulation with non-perturbative treatment of nuclear dynamics, which along with the detailed Green-Kubo formalism in Sec. (2.5) gives another approach to the lattice thermal conductivity calculation. The second part shows a toy model, one dimensional CH₂ chain to practise the thermal conductivity calculations based on LD and MD methods to save the time in the following real structures. The third part will contain the calculations and properties survey on MgO, CsF, KCaF₃, LiGaTe₂ and Lil to give a comparative benchmark of lattice thermal conductivity by *ab initio* Green-Kubo calculation. All calculations presented in this thesis are performed via FHI-aims [19, 20] and FHI-vibes [21, 22].

To my family and friends.

2. Fundamental Principles

2.1. Solution to Schrödinger Equation

Considering some well-defined collection of atoms which define the crystal of an interested material, it is desired to understand how does their energy vary with their positions. In this case, both the nucleus and electrons should be taken into consideration, which enhances the complexity of this problem. Fortunately, based on the Born-Oppenheimer approximation, nuclei can be fixed in most cases when studying the motion of electrons since the atomic nuclei are much heavier than individual electrons. Thus, the ground state energy of a collection of atoms can be computed by the solution to the Schrödinger Equation:

$$\hat{H}\Psi(\mathbf{r}_1, \mathbf{r}_2, \dots, \mathbf{r}_N) = E\Psi(\mathbf{r}_1, \mathbf{r}_2, \dots, \mathbf{r}_N) \quad (2.1.1)$$

The Hamiltonian operator consists of a sum of three terms, namely, the kinetic energy of the electrons, the interaction between each electron and the collection of atomic nuclei, and the interaction between electrons:

$$\hat{H} = -\frac{1}{2} \sum_i^N \nabla_i^2 + \hat{V}_{ext} + \sum_{i<j}^N \frac{1}{|\mathbf{r}_i - \mathbf{r}_j|}, \quad (2.1.2)$$

where

$$\hat{V}_{ext} = -\sum_{\alpha}^{N_{at}} \frac{Z_{\alpha}}{|\mathbf{r}_i - \mathbf{R}_{\alpha}|} \quad (2.1.3)$$

Here, \mathbf{r}_i is the coordinate of electron i and the charge on the nucleus at \mathbf{R}_{α} is Z_{α} . According to the *variational theorem*, the ground state Ψ and energy E_0 are given by the full minimization of the functional $E[\Psi]$ with the constraint that all wave-functions have

anti-symmetry, which means if two electrons exchange their position, the wave function has to change its sign, since electrons are fermions.

$$E[\Psi] = \int \Psi^* \hat{H} \Psi d\mathbf{r} \equiv \langle \Psi | \hat{H} | \Psi \rangle \quad (2.1.4)$$

$$E[\Psi] \geq E_0 \quad (2.1.5)$$

2.1.1. Hartree-Fock Approximation

In Hartree-Fock theory, Ψ is approximated as an antisymmetric product of the orthonormal electronic wave-function, with the form

$$\Psi_{HF} = \frac{1}{\sqrt{N!}} \det [\phi_1 \phi_2 \phi_3 \dots \phi_N] \quad (2.1.6)$$

In this case, by replacing Ψ with Ψ_{HF} in Eq.(2.1.4), the Hartree Fock energy is obtained as

$$\begin{aligned} E_{HF} = & \int \phi_i^*(\mathbf{r}) \left(-\frac{1}{2} \sum_i^N \nabla_i^2 + V_{ext} \right) \phi_i(\mathbf{r}) d\mathbf{r} \\ & + \frac{1}{2} \sum_{i,j}^N \int \frac{\phi_i^*(\mathbf{r}_1) \phi_i(\mathbf{r}_1) \phi_j^*(\mathbf{r}_2) \phi_j(\mathbf{r}_2)}{|\mathbf{r}_i - \mathbf{r}_j|} d\mathbf{r}_1 d\mathbf{r}_2 \\ & - \frac{1}{2} \sum_{i,j}^N \int \frac{\phi_i^*(\mathbf{r}_1) \phi_j(\mathbf{r}_1) \phi_i(\mathbf{r}_2) \phi_j^*(\mathbf{r}_2)}{|\mathbf{r}_i - \mathbf{r}_j|} d\mathbf{r}_1 d\mathbf{r}_2, \end{aligned} \quad (2.1.7)$$

where the second integral is called *Coulomb integral* and the third one is the *exchange integral*. The minimisation of this energy expression is subject to the ortho-normalization condition

$$\int \psi_i^*(\mathbf{x}) \psi_j(\mathbf{x}) d\mathbf{x} = \delta_{ij} \quad (2.1.8)$$

and gives the Hartree-Fock equations

$$\left[-\frac{1}{2} \nabla^2 + v_{ext}(\mathbf{r}) + \int \frac{\rho(\mathbf{r}')}{|\mathbf{r} - \mathbf{r}'|} d\mathbf{r}' \right] \phi_i(\mathbf{r}) + \int v_X(\mathbf{r}, \mathbf{r}') \phi_i(\mathbf{r}') d\mathbf{r}' = \varepsilon_i \phi_i(\mathbf{r}), \quad (2.1.9)$$

where v_X represents the non-local exchange potential given as[23]:

$$\int v_X(\mathbf{r}, \mathbf{r}') \phi_i(\mathbf{r}') d\mathbf{r}' = - \sum_j^N \int \frac{\phi_j(\mathbf{r}) \phi_j^*(\mathbf{r}')}{|\mathbf{r} - \mathbf{r}'|} \phi_i(\mathbf{r}') d\mathbf{r}' \quad (2.1.10)$$

It should be noticed that this expression is still an approximation to the real physical picture.

2.2. Density Functional Theory

The discussion above shows that the ground state energy can be approximately computed by solving the Schrödinger equation and determining the 3N dimensional wave-function, which however involves a large computation and memory cost. This problem can be circumvented by expressing the energy as a functional of charge density which reduces the problem to a 3-dimensional one according to the Hohenberg-Kohn theorem.

2.2.1. Hohenberg-Kohn theorems

The field of Density Functional Theory(DFT) is based on the two Hohenberg-Kohn theorems[24]:

Theorem I *For any system of interacting electrons in an external potential V_{ext} , the potential is determined uniquely (up to a constant) by the ground-state density.*

Since the total number of electrons can also be calculated by the integration of the charge density over all space, this statement immediately gives that the electron density uniquely determines the Hamiltonian operator and thus the energy of the system is controlled by the ground-state density.

Theorem II *A universal functional for the energy in terms of the density can be defined such that the exact ground-state energy is the global minimum of this functional with the ground-state density.*

The second theorem establishes a variational principle that the ground-state energy can be obtained by minimising the functional

$$\delta \left[E[\rho] - \mu \left(\int \rho(\mathbf{r}) d\mathbf{r} - N \right) \right] = 0. \quad (2.2.1)$$

According to Eq.(2.1.1), $E[\rho]$ is given as

$$E[\rho] = T[\rho] + V_{ext}[\rho] + V_{ee}[\rho] \quad (2.2.2)$$

with the trivial external potential term

$$V_{ext}[\rho] = \int \hat{V}_{ext} \rho(\mathbf{r}) d\mathbf{r}. \quad (2.2.3)$$

Here $E[\rho]$ is the ground-state total energy subject to the constraint that the density contains N electrons and μ is the chemical potential. Hence, the associated Euler-Lagrange equation can be written as

$$\mu = \frac{\delta E[\rho]}{\delta \rho(\mathbf{r})} = V_{ext}(\mathbf{r}) + \frac{\delta F_{HK}[\rho]}{\delta \rho(\mathbf{r})}, \quad (2.2.4)$$

where

$$F_{HK}[\rho] = T[\rho] + V_{ee}[\rho] \quad (2.2.5)$$

is not explicitly known. Note that $F_{HK}[\rho]$ is independent from the external potential, which means it is a *universal functional* of $\rho(\mathbf{r})$ and once it has an explicit form, any system could be solved. In addition, this theorem restrict DFT to be a ground-state theory.

2.2.2. Kohn-Sham Method

Kohn and Sham proposed to approximate the kinetic and electron-electron functionals by N non-interacting electrons ϕ_i . Accordingly, their kinetic energy and the charge density can be expressed as

$$T_s[\rho] = -\frac{1}{2} \sum_i^N \langle \phi_i | \nabla^2 | \phi_i \rangle \quad (2.2.6)$$

and

$$\rho(r) = \sum_i \rho_i(r) = \sum_i \phi_i^*(r) \phi_i(r). \quad (2.2.7)$$

It should be noticed that this is just the kinetic energy for non-interacting KS particles. Similarly, based on the Coulomb integral from Eq.(2.1.7) and Eq.(2.2.7), the electron-electron interaction is approximated using the classical Coulomb interaction or Hartree potential for non-interacting electrons:

$$V_H[\rho] = \frac{1}{2} \int \frac{\rho(\mathbf{r}_1) \rho(\mathbf{r}_2)}{|\mathbf{r}_1 - \mathbf{r}_2|} d\mathbf{r}_1 d\mathbf{r}_2. \quad (2.2.8)$$

Moreover, the total Kohn-Sham functional is composed of the kinetic energy, the external energy, Hartree potential which describes the interaction between electrons, exchange-correlation energy, shown as follows:

$$E[\rho] = T_s[\rho] + V_{ext}[\rho] + V_H[\rho] + E_{xc}[\rho], \quad (2.2.9)$$

where the exchange-correlation functional is defined as:

$$E_{xc}[\rho] = (T[\rho] - T_s[\rho]) + (V_{ee}[\rho] - V_H[\rho]), \quad (2.2.10)$$

which means it includes all many-body effects, i.e., the non-classical kinetic energy and the non-classical electron-electron interaction. To be more specific, E_{xc} contains both the error made by using $T_s[\rho]$ instead of $T[\rho]$ and the error made in treating the electron-electron interaction as Coulomb repulsion but neglecting the non-classical term. The minimisation of the total functional by means of variation principle and Lagrangian multipliers under the constraints of mutual orthonormality of the orbitals results in the KS equation,

$$\left[-\frac{\nabla^2}{2} + V_{ext}(r) + V_H(r) + V_{xc}(r) \right] \phi_i(r) = \epsilon_i \phi_i(r). \quad (2.2.11)$$

Comparing Eq.(2.2.11) with Eq.(2.1.9), it shows that they share the same structures except that the non-local exchange potential v_X in Hartree-Fock equations is replaced by the local exchange-correlation potential V_{xc} in Kohn-Sham equations. It should be noted that ϵ_i are not energy eigenvalues but only Lagrangian multipliers. In addition, the solutions to Kohn-Sham equations are independent single-electron wave functions that depend only on three spatial variables.

2.2.3. Exchange-Correlation Functional

In order to solve the Kohn-Sham equations exactly, explicit expression of xc functionals has to be known. However, since the functional is universal, which means it does not depend on any particular system, the functional could be approximated by determining the exact properties of that universal functional in a number of systems. Various E_{xc} functionals are categorized according to their complexity in Fig.(2.1) by Perdew and this is known as "Jacob's ladder".

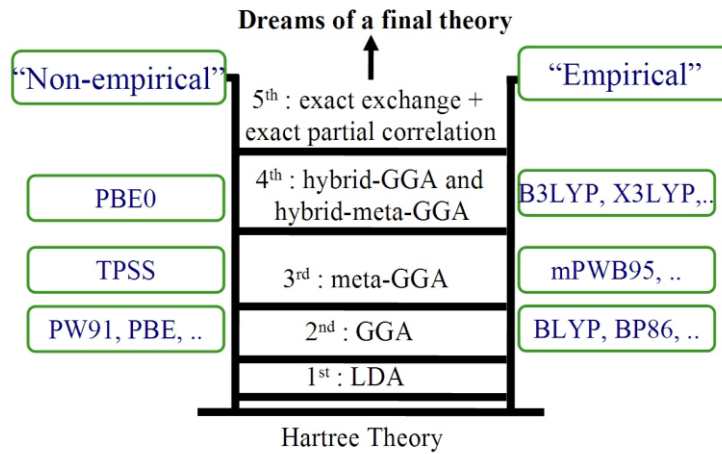


Figure 2.1.: Schematic diagram of "Jacob's ladder" of exchange-correlation functionals with 5 rungs showing some of the most common functionals. Fig. from Ref [25, 26].

Local-density Approximation(LDA)

This approximation is based on the homogeneous electron gas, as first studied by Thomas and Fermi in the early 1920's[27]. It assumes that all electrons in an infinitesimal volume are subject to one constant external potential and the charge density is constant. Then for a real inhomogeneous system, the integral over every infinitesimal volumes with different charge density gives the total exchange-correlation energy functional,

$$E_{xc}^{LDA}[\rho] \approx \int \rho(\mathbf{r})\varepsilon_{xc}(\rho(\mathbf{r}))d\mathbf{r} \quad (2.2.12)$$

where ε_{xc} indicates the exchange and correlation energy per particle of a uniform electron gas of density ρ .

The LDA has proven to describe various properties of the system, such as structure, vibrational frequencies and elastic moduli. However, its shortcomings are also recognized, including the overestimation of the binding energies and underestimation of the energy barriers in diffusion or chemical reactions.

Generalised Gradient Approximation(GGA)

In GGA, not only the density but also its gradient is taken into consideration in the exchange-correlation functional. The typical form for a GGA functional is:

$$E_{xc} \approx \int \rho(r) \varepsilon_{xc}(\rho, \nabla \rho) dr. \quad (2.2.13)$$

There are a number of examples of GGA functionals, including PBE[28], PBEsol[29], PW91[30] and so on. Typically, GGA has a better performance than LDA on calculating the binding energy, geometries and elastic coefficient.

Hybrid Exchange Functional

A hybrid exchange–correlation functional incorporates a portion of exact Hartree Fock exchange correlation evaluated for the Kohn-Sham orbitals. One specific example is the HSE(Heyd–Scuseria–Ernzerhof)[31] exchange-correlation functional, in which the long-range part of the Hartree Fock exchange interaction is screened by applying a screened Coulomb potential into the exchange interaction.

$$E_{xc}^{\omega\text{PBEh}} = aE_x^{\text{HF,SR}}(\omega) + (1 - a)E_x^{\text{PBE,SR}}(\omega) + E_x^{\text{PBE,LR}}(\omega) + E_c^{\text{PBE}}. \quad (2.2.14)$$

Here, a is the mixing parameter, and ω is a parameter controlling the screening and $E_c^{\text{HF,SR}}(\omega)$ is the short-range Hartree-Fock exact exchange.

2.2.4. Solution to Kohn Sham Equations

It is well-known that the number of atoms is in the order of Avogadro's number. In this case, solving the Schrödinger equation for each atom is not feasible.

Bloch Theorem

The Bravais lattice is an infinite periodic array of discrete points and it can describe any crystalline solid via

$$\mathbf{R} = n_1 \mathbf{a}_1 + n_2 \mathbf{a}_2 + n_3 \mathbf{a}_3, \quad (2.2.15)$$

where \mathbf{a}_1 , \mathbf{a}_2 and \mathbf{a}_3 are called primitive vectors and n are integers. The solution to the Schrödinger equation for periodic system, for instance solids, must satisfy Bloch's theorem, where the solution should have the plane-wave form

$$\phi_{n\mathbf{k}}(\mathbf{r}) = \exp(i\mathbf{k} \cdot \mathbf{r}) u_{n\mathbf{k}}(\mathbf{r}) \quad (2.2.16)$$

where $u_{n\mathbf{k}}(\mathbf{r})$ has the same periodicity as the supercell,

$$u_{n\mathbf{k}}(\mathbf{R} + \mathbf{r}) = u_{n\mathbf{k}}(\mathbf{r}) \quad (2.2.17)$$

for all \mathbf{R} in the Bravais lattice. Combining the Eqs.(2.2.16) and (2.2.17) gives that

$$\phi_{n\mathbf{k}}(\mathbf{r} + \mathbf{R}) = \exp(i\mathbf{k} \cdot \mathbf{R}) \phi_{n\mathbf{k}}(\mathbf{r}). \quad (2.2.18)$$

Here, the index \mathbf{k} indicates a set of plane waves within each primitive unit cell and the index n is known as the band index. For a given \mathbf{k} , there will be many independent eigenstates of H and thus many solutions with discretely spaced eigenvalues, which could be labeled by this second quantum number n . Fortunately, solids contain some periodicity and thus the calculation could be reduced to the unit cell by applying the Born von Karman periodic boundary condition,

$$\phi(\mathbf{r} + N_i \mathbf{a}_i) = \phi(\mathbf{r}), \quad i = 1, 2, 3 \quad (2.2.19)$$

where the three primitive lattice vectors \mathbf{a}_i define the Bravais lattice and N_i is an integer of order $N^{\frac{1}{3}}$, where $N = N_1 N_2 N_3$ is the total number of primitive cells in the crystal. Substitution of the boundary condition to Bloch's theorem leads to the general form for allowed Bloch wave vectors

$$\mathbf{k} = \sum_{i=1}^3 \frac{m_i}{N_i} \mathbf{b}_i, \quad m_i \text{ is integer.} \quad (2.2.20)$$

Here, \mathbf{b}_i are reciprocal lattice vectors satisfying the relation

$$\mathbf{b}_i \cdot \mathbf{a}_j = 2\pi\delta_{ij}. \quad (2.2.21)$$

Basis Set

In practice, the Kohn Sham equation(Eq. 2.2.11) can only be solved self-consistently by picking a basis set to expand the electronic Kohn-Sham eigenfunctions ϕ_i as

$$\phi_i = \sum_j c_{ij}\zeta_j(\mathbf{r}). \quad (2.2.22)$$

This particular work is based on the full algorithmic framework embodied in the Fritz Haber Institute “ab initio molecular simulations” (*FHI-aims*) computer program package[20], which utilizes numeric atom-centered orbital(NAO) as basis functions

$$\zeta_i(\mathbf{r}) = \frac{u_i(r)}{r}Y_{lm}(\Omega). \quad (2.2.23)$$

Here, the basis function consists of the numerically tabulated radial function $u_i(r)$ and complex spherical harmonics $Y_{lm}(\Omega)$. Combining the exponential part from the Bloch theorem gives the final expression for the Bloch-like basis set

$$\chi_{i,\mathbf{k}}(\mathbf{r}) = \sum_N \exp[i\mathbf{k} \cdot \mathbf{T}(N)] \cdot \zeta_i[\mathbf{r} - \mathbf{R}_{\text{at}} + \mathbf{T}(N)] \quad (2.2.24)$$

provided for periodic calculations in FHI-aims. $\mathbf{T}(N)$ represents the translation vector between the unit cell and its periodic images, and \mathbf{R}_{at} are the coordinates of the nucleus for basis function in the unit cell. The above eq. (2.2.24) implies that only finite k-grid are used in practical calculations and the convergence of the quantities of interest with respect to this numerical parameter should always be checked.

2.3. Dynamic lattice model

2.3.1. Harmonic approximation

Compared with a static lattice model assumed in the previous sections, now the nucleus does have the flexibility to move at the sites \mathbf{R} of a Bravais lattice. If the each ion does

not deviate much from its equilibrium position compared with the inter-ionic spacing, the harmonic approximation can be applied to model this motion. To be more specific, we consider an ion sitting at \mathbf{R} and a displacement $\mathbf{r}(\mathbf{R})$ around its equilibrium, leading to the instantaneous position $\mathbf{r}(\mathbf{R})$,

$$\mathbf{r}_{\mathbf{R}} = \mathbf{R} + \mathbf{u}_{\mathbf{R}}. \quad (2.3.1)$$

The potential-energy surface(PES) for the nuclei, on which the nuclei move, can be approximated by a Taylor expansion of the total energy, provided by DFT calculations, for small displacement around the equilibrium positions. Within this Taylor expansion, the first derivative term cancels since there is no net force on any atom in equilibrium. One thus obtains

$$E(u_I) = E_0 + \frac{1}{2} \sum_{I\alpha, J\beta} \frac{\partial^2 E}{\partial u_I^\alpha \partial u_J^\beta} u_I^\alpha u_J^\beta, \quad (2.3.2)$$

with the Hessian matrix

$$\Phi_{IJ} = \frac{\partial^2 E}{\partial u_I^\alpha \partial u_J^\beta} = - \lim_{\epsilon \rightarrow 0} \frac{F_J(u_I^0 + \epsilon d_I)}{\epsilon}. \quad (2.3.3)$$

The respective equation of motion is solved by the plane-wave ansatz

$$u_{I\alpha} = \frac{A}{\sqrt{M_I}} \epsilon_{I\alpha}(\mathbf{q}, s) e^{i(\mathbf{q} \cdot \mathbf{R}_I - \omega t)}. \quad (2.3.4)$$

Here, $\epsilon_{I\alpha}$ is a polarization vector of the normal mode that describes the direction in which ions move. Φ_{IJ} is also called force-constant matrix and represents the response of atom I to the displacement of atom J in some direction β . In this work, this second-order derivative will be computed numerically by *finite differences* method. However, the periodic images $R_{J'}$ have to be accounted for due to the periodic boundary condition. In this case, the Hessian is in principle a matrix with infinite size. In non-ionic crystals, however, the coupling between two atoms I and J quickly decays with their distance R_{IJ} , so the Hessian can be computed with finite supercells, the size convergence of which must be accurately inspected. The mass-reduced Fourier transformation of the force constant matrix gives the so-called dynamical matrix D_{IJ} , shown as

$$D_{IJ}(\mathbf{q}) = \sum_{J'} \frac{e^{i(\mathbf{q} \cdot \mathbf{R}_{JJ'})}}{\sqrt{M_I M_J}} \Phi_{IJ'}, \quad (2.3.5)$$

which determines the equation of motion for each reciprocal vector \mathbf{q} in the periodic array of atoms[32],

$$\mathbf{D}(\mathbf{q}) \epsilon_s(\mathbf{q}) = \omega_s^2(\mathbf{q}) \epsilon_s(\mathbf{q}), \quad s = 1, 2, 3, \dots, 3N. \quad (2.3.6)$$

The eigenfrequency in the harmonic approximation is expressed as

$$\omega_s^2(\mathbf{q}) = \sum_{IJ,\alpha\beta} \frac{\epsilon_{I,s}^{*\alpha}(\mathbf{q})\epsilon_{J,s}^\beta(\mathbf{q})}{\sqrt{M_I M_J}} \Phi_{IJ}^{\alpha\beta} e^{i\mathbf{q}\cdot(\mathbf{R}_J - \mathbf{R}_I)}, \quad (2.3.7)$$

which implies that if a primitive cell has N atoms, then there will be $3N$ solutions at each \mathbf{q} point. Each real eigenvalue $\omega_s(\mathbf{q})$ represents a mode or phonon branch and the set of them constitutes the dispersion relation and the phonon spectrum, in which the lowest three branches in solids are called *acoustic mode*, which means the translation motion of the molecule, while other $(3N-3)$ branches represent the optical modes. Moreover, the density of state(DOS) is a significant quantity, that can be calculated by integrating the number of states in an infinitesimal energy window $[\omega, \omega + d\omega]$ as:

$$g(\omega) = \sum_s \int \frac{d\mathbf{q}}{(2\pi)^3} \delta(\omega - \omega(\mathbf{q})). \quad (2.3.8)$$

The DOS allows to compute other thermodynamic quantities, for instance, the *Helmholtz free energy*, from which the heat capacity can further be calculated.

$$F^{\text{ha}}(T, V) = \int d\omega g(\omega) \left(\frac{\hbar\omega}{2} + k_B T \ln \left(1 - e^{-\frac{\hbar\omega}{k_B T}} \right) \right) \quad (2.3.9)$$

$$C_V = -T \left(\frac{\partial^2 F^{\text{ha}}(T, V)}{\partial T^2} \right)_V. \quad (2.3.10)$$

2.3.2. Beyond Harmonic approximation

In the Born-Oppenheimer approximation, the vibrational properties of molecules and solids are determined by their electronic structure through the dependence of the ground-state energy on the coordinates of the atomic nuclei. Further, in the harmonic approximation(HA), where the amplitudes of atomic vibrations at low temperature are much smaller than inter-atomic distances, it is assumed that the properties of solids can be calculated by only considering the dominant non-vanishing quadratic term in the expansion of the total energy about its equilibrium value. However, it has been noticed that some phenomena, for example, the thermal expansion can not be determined by this term.

In the HA, vibrational frequencies do not depend on inter-atomic distances, so that

the vibrational contribution to the crystal internal energy does not depend on volume. Consequently, specific heats under constant pressure and constant volume are the same, and equilibrium volume of a crystal does not depend on temperature. To be more specific, for a harmonic crystal the equilibrium size or the lattice constant is independent on temperature while in fact the elastic constants depend on both volume and temperature, and the elastic constants under the adiabatic and isothermal condition give different values. In this case, higher-order terms, i.e. the anharmonic terms in the expansion of the total energy need to be accounted for. A proper account of anharmonic effects on the static and dynamical properties of materials would require the calculation of phonon-phonon interaction coefficients for all modes in the Brillouin zone, which will be discussed in the next two sections.

Here, the generalized harmonic approximation, i.e. *quasi harmonic approximation*(QHA) accounts for the volume-dependence of both the total energy $E_{tot}(V)$ and the force constant $\Phi_{IJ}^{\alpha\beta}(V)$, which correct for the above mentioned deficiencies without any explicit calculation of anharmonic interaction coefficients. In this case, the Helmholtz free energy can be expressed as

$$F(T, V) \approx E_{tot}(V) + F^{qha}(T, V) \quad \text{with} \quad F^{qha}(T, V) = F^{ha}\left(T, \Phi_{IJ}^{\alpha\beta}(V)\right), \quad (2.3.11)$$

where the equilibrium volume V_0 corresponds to the minimum of the total energy of the system $E_{tot}(V)$. Once the Helmholtz free energy $F(T, V)$ is computed at different volumes and temperatures, thermodynamic data including equilibrium free energy $E_{tot}(V)$, equilibrium volume V_0 , bulk modulus B , and the derivative of the bulk modulus with respect to pressure B_0 can be extracted straightforwardly by fitting $F(T, V)$ at different volumes and temperatures to the Birch-Murnaghan (BM) function

$$F(V) = F_{eq} + \frac{BV_0}{B_p} \left[\frac{(V_0/V)^{B_p}}{B_p - 1} + 1 \right] - \frac{V_0 B}{B_p - 1}. \quad (2.3.12)$$

As an example, the results of the final fitting for silicon are depicted in Fig. (2.2), where points represent calculated data and solid lines indicate the Birch-Murnaghan equation of state fits. Equilibrium volumes at each temperature are connected by solid black line, which allows to compute the thermal expansion coefficient $V_0(T)$ as

$$\alpha(T) = \frac{1}{3V_0(T)} \left(\frac{\partial V_0(T)}{\partial T} \right)_V \quad (2.3.13)$$

The right-shift of the equilibrium volume indicates a positive thermal expansion coefficient, which agrees with the intuition that matter tends to expand under high temperature. However, there exist some exceptions, for example, that diamond and zinc-blend semiconductors have a negative thermal expansion coefficient at 100K.[33, 34]

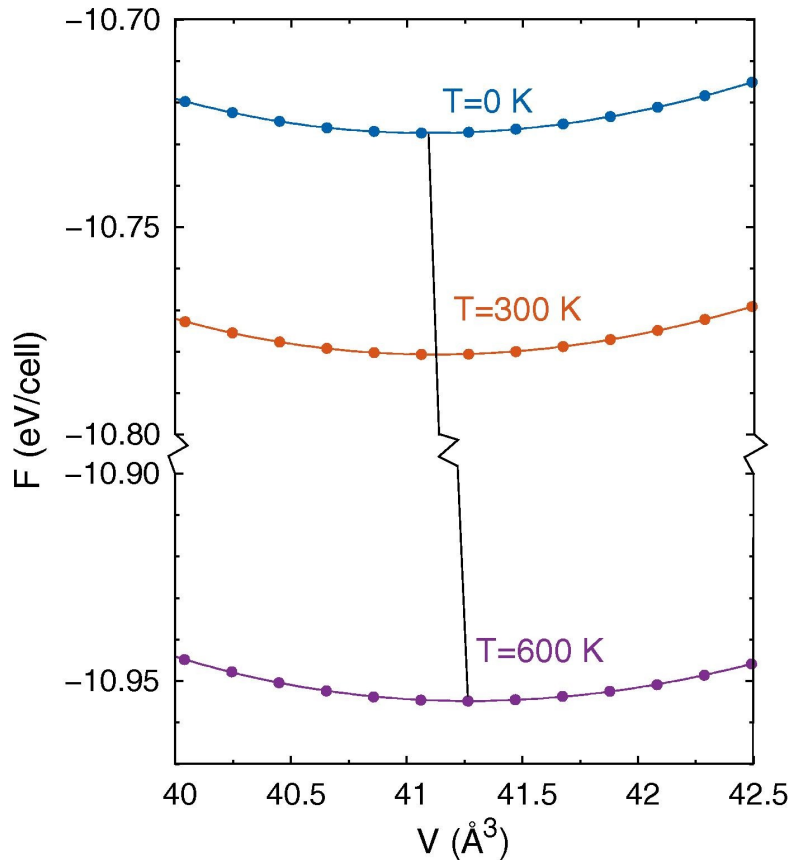


Figure 2.2.: Free energy and volume data fitted using Birch-Murnaghan function for different temperatures for Si. Fig. from Ref.[35]

In order to assess temperature dependence of volumes and lattice constants, the volume expansion coefficient is defined as thermodynamic derivative

$$\alpha(T) = -\frac{1}{3B} \left(\frac{\partial^2 F(T, V)}{\partial T \partial V} \right)_{V_0(T)} \quad (2.3.14)$$

whereby B is the bulk modulus which measures the resistance of the material to compression. With the static limit $V_0(T) \rightarrow V_0$, inserting the harmonic free energy defined in Eq. (2.3.9) into the above Eq. (2.3.14) yields a more practical expression

$$\alpha = \frac{1}{3B_0} \sum_{\mathbf{q},s} \left(-\frac{\partial \hbar\omega_s(\mathbf{q})}{\partial V} \right) \frac{\partial n_s^{eq}(\mathbf{q})}{\partial T} = \frac{1}{3B_0} \sum_{\mathbf{q},s} \frac{\hbar\omega_s(\mathbf{q})\gamma_s(\mathbf{q})}{V} \frac{\partial n_s^{eq}(\mathbf{q})}{\partial T} = \frac{\gamma C_V}{3B_0}. \quad (2.3.15)$$

with the mode-specific *Grüneisen* parameter $\gamma_s(\mathbf{q})$ and an average Grüneisen parameter defined as

$$\gamma_s(\mathbf{q}) = -\frac{V}{\omega_s(\mathbf{q})} \frac{\partial \omega_s(\mathbf{q})}{\partial V} \quad (2.3.16)$$

$$\gamma = \frac{\sum_{\mathbf{q},s} \gamma_s(\mathbf{q}) c_s(\mathbf{q})}{\sum_{\mathbf{q},s} c_s(\mathbf{q})}. \quad (2.3.17)$$

Apart from the equilibrium properties, transport properties are also dominated by the anharmonic terms. For instance, the thermal conductivity of a perfect harmonic crystal for which the phonon states are stationary states should be infinite, in analogous to the fact that electrons in a perfect periodic potential would have infinite electric conductivity. This contradiction can be cleared by the fact that there exist lattice imperfections and impurities in real crystals which results in the scattering centers for the phonons and the limitation of the thermal current. Even in a conceptual perfect crystal, the stationary states of the harmonic Hamiltonian are only an approximation to the real full anharmonic Hamiltonian, which means phonons will interact with each other in the course of time. The effect of anharmonicity can be modeled as a perturbation to the harmonic Hamiltonian H_0 , which causes transitions from one harmonic eigenstate to another and thus the creation, destruction and scattering of phonons.

The expression of the total energy retaining cubic anharmonic terms is shown explicitly as:

$$E_{tot} = E_0 + \frac{1}{2} \sum_{IJ,\alpha\beta} \Phi_{IJ}^{\alpha\beta} u_I^\alpha u_J^\beta + \frac{1}{6} \sum_{IJK,\alpha\beta\gamma} \Psi_{IJK}^{\alpha\beta\gamma} u_I^\alpha u_J^\beta u_K^\gamma, \quad (2.3.18)$$

with the third-order force constants

$$\Psi_{IJK}^{\alpha\beta\gamma} = \frac{\partial^3 E}{\partial R_I^\alpha \partial R_J^\beta \partial R_K^\gamma}. \quad (2.3.19)$$

It should be noticed that we here only consider the non-vanishing anharmonic cubic term, again assuming that only low-order terms matter for small oscillations around equilibrium sites. In practice, the anharmonic effect can be evaluated by *perturbation theory* if the anharmonic term is small compared with the harmonic one. For this purpose, also the third order term can be calculated by *finite differences* as

$$\Psi_{IJK}^{\alpha\beta\gamma} = \frac{\partial \Phi_{IJ}}{\partial R_K^\gamma} \approx \frac{\Phi_{IJ}^{\alpha\beta}(\delta R_K^\gamma) - \Phi_{IJ}}{\delta R_K^\gamma}. \quad (2.3.20)$$

Then perturbation theory yields an extra term compared with the harmonic approximation in Eq.(2.3.7):

$$\omega_s^2(\mathbf{q}) = \omega_s^2(\mathbf{q}) + \sum_{IJ,\alpha\beta} \frac{\epsilon_{I,s}^{*\alpha}(\mathbf{q})\epsilon_{J,s}^\beta(\mathbf{q})}{\sqrt{M_I M_J}} \left(\sum_{\gamma,K} \Psi_{IJK}^{\alpha\beta\gamma} u_K^\gamma \right) e^{i\mathbf{q}\cdot(\mathbf{R}_J - \mathbf{R}_I)}. \quad (2.3.21)$$

2.3.3. Phonon interaction and thermal conductivity

As discussed in Sec.(2.3.1) and Sec. (2.3.2), phonons do not interact with each other and can live forever within the harmonic approximation. In addition, anharmonic effects manifest themselves as phonon-phonon interaction described by the phonon self-energy $\Delta(\omega) - i\Gamma(\omega)$ [36]. Among the complex function, the real part $\Delta(\omega)$ is associated with the change of the frequency due to scattering by other phonons, and thus is responsible for the temperature dependence of the phonon frequency, and the imaginary part $i\Gamma(\omega)$ gives the probability of phonon decay, indicating the reciprocal of the phonon lifetime[37]. The strength of interaction between the three phonons, namely s, s', s'' involved in the scattering, can be represented by the Fourier transform of the third-order forces constant:

$$\begin{aligned} \Psi_{s,s',s''}(\mathbf{q}, \mathbf{q}', \mathbf{q}'') &= \frac{1}{3!\sqrt{N_0}} \sum_{IJK,\alpha\beta\gamma} \epsilon_{I,s}^\alpha(\mathbf{q})\epsilon_{J,s'}^\beta(\mathbf{q}')\epsilon_{K,s''}^\gamma(\mathbf{q}'') \\ &\times \sqrt{\frac{\hbar}{2M_I\omega_s(\mathbf{q})}} \sqrt{\frac{\hbar}{2M_J\omega_{s'}(\mathbf{q}')}} \sqrt{\frac{\hbar}{2M_K\omega_{s''}(\mathbf{q}'', s'')}} \\ &\times \Psi_{IJK}^{\alpha\beta\gamma} e^{i\mathbf{q}\cdot\mathbf{R}_I} e^{i\mathbf{q}'\cdot\mathbf{R}_J} e^{i\mathbf{q}''\cdot\mathbf{R}_K} \Delta(\mathbf{q}+\mathbf{q}'+\mathbf{q}''). \end{aligned} \quad (2.3.22)$$

The above-mentioned imaginary part of the self-energy can be now expressed using many-body perturbation theory as

$$\Gamma_s(\omega) = \frac{18\pi}{\hbar^2} |\Phi_{-ss's''}|^2 \{ (n_{s'} + n_{s''} + 1) \delta(\omega - \omega_{s'} - \omega_{s''}) + (n_{s'} - n_{s''}) [\delta(\omega + \omega_{s'} - \omega_{s''}) - \delta(\omega - \omega_{s'} + \omega_{s''})] \}, \quad (2.3.23)$$

where $\Delta(\mathbf{q} + \mathbf{q}' + \mathbf{q}'') = 1$ when $\mathbf{q} + \mathbf{q}' + \mathbf{q}''$ is a reciprocal lattice vector, and is zero otherwise. Here, N_0 is number of unit cells in the crystal and n_s is the phonon occupation number at the equilibrium. Since phonons follow the Bose-Einstein distribution, it follows that

$$n_s = \frac{1}{\exp(\hbar\omega_s/k_B T) - 1}. \quad (2.3.24)$$

Finally, the linewidth of the phonon mode s is just $2\Gamma_s(\omega)$ which can also be measured by Raman spectroscopy[38] and the phonon lifetime has a simple reciprocal form:

$$\tau_s = \frac{1}{2\Gamma_s(\omega_s)}. \quad (2.3.25)$$

It has been proven that the lattice thermal conductivity can be directly computed by a full solution of the linearized phonon Boltzmann equation(LPBE).[39] Even simpler, Togo et al. [40] also showed that the lattice thermal conductivity is proportional to phonon lifetimes τ_s in the single mode relaxation time (SMRT) method via

$$\kappa = \frac{1}{NV_0} \sum_s C_s \mathbf{v}_s \otimes \mathbf{v}_s \tau_s^{\text{SMRT}}, \quad (2.3.26)$$

where V_0 is the volume of a unit cell, and v_s and τ_s^{SMRT} are the group velocity and SMRT of the phonon mode s , respectively. Based on the SMRT approximation, every phonon mode is assigned a relaxation time corresponding to the net effect of different scattering mechanisms[41]. The single mode relaxation time is assumed to be the phonon lifetime, which means

$$\tau_s^{\text{SMRT}} = \tau_s. \quad (2.3.27)$$

C_s is the mode dependent heat capacity defined as

$$C_s = k_B \left(\frac{\hbar\omega_s}{k_B T} \right)^2 \frac{\exp(\hbar\omega_s/k_B T)}{[\exp(\hbar\omega_s/k_B T) - 1]^2}. \quad (2.3.28)$$

The phonon group velocity is simply given by the derivative of the eigenfrequency with respect to the wave-vector:

$$\mathbf{v}_s(\mathbf{q}) = \frac{\partial \omega_s(\mathbf{q})}{\partial \mathbf{q}} = \frac{1}{2\omega} \left\langle \epsilon_s(\mathbf{q}) \left| \frac{\partial D(\mathbf{q})}{\partial \mathbf{q}} \right| \epsilon_s(\mathbf{q}) \right\rangle. \quad (2.3.29)$$

2.4. Molecular dynamics

Molecular dynamics (MD) is a computational approach exploring the dynamical properties of a system defined by the Hamiltonian

$$\mathcal{H}(\mathbf{r}, \mathbf{p}) = \sum_I \left[\frac{\mathbf{p}_I^2}{2M_I} + \mathcal{V}(\mathbf{r}_I) \right] \quad (2.4.1)$$

where M_I is the atomic mass and \mathcal{V} is a many-body potential obtained by an empirical force-field or DFT calculation. The dynamical evolution of a general N-particle system is described by the classical equations of motion

$$M_I \ddot{\mathbf{r}}_I = \mathbf{F}_I(\mathbf{r}_I, \dots, \mathbf{r}_N, \dot{\mathbf{r}}_I), \quad (2.4.2)$$

which are solved numerically starting from a given initial condition $\{\mathbf{r}(t_0), \mathbf{p}(t_0)\}$. The trajectories generated by this means are used to extract micro- and macroscopic observables. This method has been widely used to investigate condensed phase systems. For example, the thermal decomposition of the energetic material nitromethane (CH_3NO_2) is studied by MD implying different chemical reaction mechanism under high temperature(3000K) and lower temperature(2000K).[42] Compared with the standard MD technique, which is based on the use of empirical interatomic potential functions parametrized to experimental data, ab initio molecular dynamics(**aiMD**), does not require an empirical interaction potential as input, but utilizes interatomic forces computed directly from the electronic structure, i.e. DFT calculation discussed in section 2.2:

$$\mathbf{F}_I = -\frac{dE_{tot}}{d\mathbf{r}_I}, \quad (2.4.3)$$

where the total energy E_{tot} is determined from the standard DFT and \mathbf{r}_I indicates the nuclear degrees of freedom.

aiMD has been successfully demonstrated in studies of diffusional properties[43, 44, 45, 46, 47] phase transition[48] etc. However **aiMD** simulations are often limited to a few hundred atoms and a short, sub-nanosecond physical timescale, which limits the accessible statistics and thermodynamics. For instance, the number of diffusion events accessible is limited to non-rare events.[49]

Phase space

According to Newton's equation shown in Eq. (2.4.2), at any time t , there will be a corresponding position $\mathbf{r}(t)$ and its velocity $\mathbf{v}(t)$. Considering the relation between velocity and momenta

$$\mathbf{p}_I = M_I \mathbf{v}_I = M_I \dot{\mathbf{r}}_I, \quad (2.4.4)$$

the Newton's equation can be rewritten as

$$\mathbf{F}_I = m \mathbf{a}_I = m_i \frac{d\mathbf{v}_I}{dt} = \frac{d\mathbf{p}_I}{dt} \quad (2.4.5)$$

Therefore, the full set of $6N$ functions, $\{\mathbf{r}_1(t), \dots, \mathbf{r}_N(t), \mathbf{p}_1(t), \dots, \mathbf{p}_N(t)\}$ describes the classical dynamics of an N -particle system and can be considered as a single point in a $6N$ -dimensional space called phase space Γ , i.e. microscopic state of the system at time t . Each point in the phase space is also known as the phase space vector and can be denoted as

$$\mathbf{x} = (\mathbf{r}_1, \dots, \mathbf{r}_N, \mathbf{p}_1, \dots, \mathbf{p}_N). \quad (2.4.6)$$

In this regard, the solutions to the above Newton's Equation generate a series of points, shown as

$$\mathbf{x}_t = (\mathbf{r}_1(t), \dots, \mathbf{r}_N(t), \mathbf{p}_1(t), \dots, \mathbf{p}_N(t)), \quad (2.4.7)$$

which constitutes the *trajectory* in the phase space Γ .

Statistical mechanics provides a way to study the behavior of large numbers of atoms or molecules, where large number of configurations ensures that the statistical average $\langle A \rangle_{\text{time}}$ of the desiring physical quantities A , with

$$\langle A \rangle_{\text{time}} = \frac{1}{t_2 - t_1} \int_{t_1}^{t_2} dt A(t) \quad (2.4.8)$$

is close to the ensemble average[50] $\langle A \rangle_{\text{time}}$ with

$$\langle A \rangle_{\text{ensemble}} = \int d\Gamma \rho(r, p) A(r, p). \quad (2.4.9)$$

This method essentially integrates the equations of motion numerically and then the system moves along the trajectory in the phase space determined by such equations. Generally, both static physical quantities and dynamic phenomena could be evaluated by

molecular dynamics, including the transport of heat which will be discussed in this thesis later.

In molecular dynamics calculation, the trajectory that the system moves along is computed by solving Hamilton's equation

$$\dot{q}_i = \frac{\partial \mathcal{H}}{\partial p_i}, \quad \dot{p}_i = -\frac{\partial \mathcal{H}}{\partial q_i}, \quad (2.4.10)$$

where \mathcal{H} is the Hamiltonian which is simply the total energy of the system expressed as a function of positions and momenta, i.e. a set of generalized coordinates \mathbf{p} and their conjugate ones \mathbf{q} . The Hamilton's equations are solved numerically using a particular numerical integrator or solver for the equations of motion with a set of initial conditions, for example, the *Verlet algorithm* that as a *finite difference method* will be discussed in section 2.4.1. In addition, as it has been shown in Eq.(2.4.8, 2.4.9), the microcanonical phase space averages can be replaced by time averages over the trajectory according to

$$\langle a \rangle = \frac{\int dx a(\mathbf{x}) \delta(\mathcal{H}(\mathbf{x}) - E)}{\int dx \delta(\mathcal{H}(\mathbf{x}) - E)} = \lim_{\mathcal{T} \rightarrow \infty} \frac{1}{\mathcal{T}} \int_0^{\mathcal{T}} dt a(\mathbf{x}_t) \equiv \bar{a}. \quad (2.4.11)$$

Then phase space vectors at discrete times are generated from the initial condition \mathbf{x}_0 by the integrator with the form $\mathbf{x}_{n\Delta t}$ that are multiples of a fundamental time discretization parameter, Δt , known as the *time step*. Thus, the ensemble average of any property a can be related to the discretized time average

$$A = \langle a \rangle = \frac{1}{M} \sum_{n=1}^M a(\mathbf{x}_{n\Delta t}) \quad (2.4.12)$$

2.4.1. Verlet algorithms

The Verlet algorithm and further the velocity Verlet algorithm basically integrate the equations of motion to find the new position and momentum from the previous ones, and sample a sufficient number of microstates to obtain reliable averages. It starts from the Taylor expansion of the position of a particle at a time $t + \Delta t$ in its position, velocity and acceleration

$$\mathbf{r}_I(t + \Delta t) \approx \mathbf{r}_I(t) + \Delta t \dot{\mathbf{r}}_I(t) + \frac{1}{2} \Delta t^2 \ddot{\mathbf{r}}_I(t). \quad (2.4.13)$$

Substituting the second order in Δt based on Newton's equation in Eq.(2.4.2) gives

$$\mathbf{r}_I(t + \Delta t) \approx \mathbf{r}_I(t) + \Delta t \mathbf{v}_I(t) + \frac{\Delta t^2}{2M_I} \mathbf{F}_I(t). \quad (2.4.14)$$

Similarly,

$$\mathbf{r}_I(t - \Delta t) = \mathbf{r}_I(t) - \Delta t \mathbf{v}_I(t) + \frac{\Delta t^2}{2M_I} \mathbf{F}_I(t). \quad (2.4.15)$$

The addition of Eq.(2.4.14) and Eq.(2.4.15) gives the numerical solver known as the *Verlet algorithm*

$$\mathbf{r}_I(t + \Delta t) = 2\mathbf{r}_I(t) - \mathbf{r}_I(t - \Delta t) + \frac{\Delta t^2}{m_I} \mathbf{F}_I(t). \quad (2.4.16)$$

However, the Verlet algorithm does not explicitly evolve the velocities which can be further introduced by a variant of the *Verlet integrator*, called the *velocity Verlet algorithm*:

$$\mathbf{v}_I(t + \Delta t) = \mathbf{v}_I(t) + \frac{\Delta t}{2M_I} [\mathbf{F}_I(t) + \mathbf{F}_I(t + \Delta t)] \quad (2.4.17)$$

With Eq.(2.4.16) and Eq.(2.4.17), the position and momentum of the particle can be obtained simultaneously. Time step limits the length of the MD trajectory and the simulation and it can cause a MD simulation to become unstable with Energy increasing rapidly with time. In practice, for numerical stability and accuracy in conserving the energy, one typically needs to pick a time step that is at least one order of magnitude lower than the fastest time scale in the system. For example, if the periodicity for bond vibration is 10 fs, then the MD time step can be chosen as 0.5-1.0 fs.

2.4.2. Ensembles

Molecular dynamics is embodied with statistical mechanics for predicting macroscopic thermodynamic and dynamic observables. The statistical ensemble is an imaginary collection of systems described by the same Hamiltonian with each system in a unique microscopic state at any given instant in time. Molecular dynamics defined in Eqs.(2.4.5, 2.4.6, 2.4.7) is confined within micro-canonical ensemble where the systems hold fixed energy, volume and particle number. In such case, the so-called *Ergodic hypothesis* dominates, which means all accessible states share the same probability in the course of time, as shown in Eq.(2.4.18). $\mathcal{H}(X)$ represents the Hamiltonian for any point X in phase space and delta function make sure only the states with energy E will be considered as consistent as NVE

ensemble definition. The discrete sum $\sum_{\{X|E\}}$ denotes a sum over all states X with a fixed energy E.

$$\langle A \rangle = \frac{\sum_{\{X|E\}} A(X)}{\sum_{\{X|E\}} 1} = \frac{\sum_X A(X) \delta[\mathcal{H}(X) - E]}{\sum_X \delta[\mathcal{H}(X) - E]} = \bar{A}. \quad (2.4.18)$$

In addition, MD can be extended to canonical ensembles where other physical quantities, namely, number of particles, volume and temperature are fixed or whose average value is controlled externally. Specifically, the temperature as a system parameter could be manipulated by coupling the system to a heat bath. The canonical ensemble average reads as

$$\langle A \rangle_{NVT} = \frac{1}{N!Z} \sum_X A(X) e^{-\beta \mathcal{H}(X)} \quad (2.4.19)$$

with the partition function describing measuring the number of microscopic states in the phase space accessible within a given ensemble

$$Z(N, V, T) = \frac{1}{N!} \sum_X e^{-\beta \mathcal{H}(X)}. \quad (2.4.20)$$

Here β is the Boltzmann factor and N is the number of particles. In addition, the *virial theorem* bridges the ensemble averages and macroscopic thermodynamic observables, stating that,

$$\left\langle x_i \frac{\partial \mathcal{H}}{\partial x_j} \right\rangle = kT \delta_{ij}, \quad (2.4.21)$$

where the average is taken with respect to a microcanonical ensemble. If x_i is picked as momentum p_i and $\mathcal{H} = \sum_i \mathbf{p}_i^2 / 2m_i + U(\mathbf{r}_1, \dots, \mathbf{r}_N)$, then the kinetic energy of each particle at equilibrium must be $\frac{1}{2}k_B T$. Summing up all N particles gives the *Equipartition Theorem*

$$\sum_{i=1}^{3N} \left\langle \frac{p_i^2}{2m_i} \right\rangle = \sum_{i=1}^{3N} \left\langle \frac{1}{2} m_i v_i^2 \right\rangle = \frac{3}{2} N k_B T \quad (2.4.22)$$

It should be noted that the canonical ensemble average is more useful when comparing to measurements, since the temperature can be controlled in the experiment.

2.4.3. Langevin thermostat

Dealing with physics or chemistry problem often requires to consider the environment that particles or molecules live in, which is referred to as *bath*. The Hamiltonian for generalized

coordinates r and its conjugate momentum p for a classic system in the absence of the bath can be written simply as

$$\mathcal{H}(r, p) = \frac{p^2}{2\mu} + V(r), \quad (2.4.23)$$

where μ is the mass associated with r and $V(r)$ is the potential independent of the bath. If the system is coupled to the bath, the total potential is

$$U(r, y_1, \dots, y_n) = V(r) + U_{\text{bath}}(r, y_1, \dots, y_n), \quad (2.4.24)$$

where r is the system coordinate and y is the bath coordinate, and U_{bath} involves both the coupling terms between the system and the bath, and harmonic potential terms describing the interactions among the bath. A real bath is often characterized by a continuous distribution of frequencies $I(\omega)$ called the spectral density or density of states obtained by taking the Fourier transform of the velocity autocorrelation function. This continuous distribution of frequencies can be approximated by the sum of harmonic oscillator spectral functions since the motion of the real bath is dominated by small displacements from an equilibrium point described by discrete frequencies. The full Hamiltonian in the harmonic bath approximation can thus be written as

$$\mathcal{H} = \frac{p^2}{2\mu} + V(r) + \sum_{\alpha=1}^n \left[\frac{p_{\alpha}^2}{2m_{\alpha}} + \frac{1}{2} \sum_{\alpha=1}^n m_{\alpha} \omega_{\alpha}^2 x_{\alpha}^2 \right] + r \sum_{\alpha=1}^n g_{\alpha} x_{\alpha}, \quad (2.4.25)$$

where x is a linear normal-mode transformation of the coordinates y , ω is the bath frequency and the last term represents the bilinear coupling to the coordinate r .

The *generalized Langevin equation* (GLE) can be derived from the equation of motion generated by the above full Hamiltonian, shown as

$$\mu \ddot{r} = -\frac{dW}{dr} - \int_0^t d\tau \dot{r}(\tau) \zeta(t - \tau) + R(t), \quad (2.4.26)$$

with the *dynamic friction kernel* $\zeta(t)$

$$\zeta(t) = \sum_{\alpha} \frac{g_{\alpha}^2}{m_{\alpha} \omega_{\alpha}^2} \cos \omega_{\alpha} t, \quad (2.4.27)$$

the *random force*

$$R(t) = -\sum_{\alpha} g_{\alpha} \left[\left(x_{\alpha}(0) + \frac{g_{\alpha}}{m_{\alpha} \omega_{\alpha}^2} r(0) \right) \cos \omega_{\alpha} t + \frac{p_{\alpha}(0)}{m_{\alpha} \omega_{\alpha}} \sin \omega_{\alpha} t \right], \quad (2.4.28)$$

and the potential of mean force acting on the system coordinate $W(r)$

$$W(r) = V(r) - \sum_{\alpha} \frac{g_{\alpha}^2}{m_{\alpha}\omega_{\alpha}^2} r^2. \quad (2.4.29)$$

Simulations based on Langevin equation require much less computational effort compared to explicitly considering a bath. In addition, the Langevin equation provides a simple and efficient thermostat for generating the canonical samples which can be used in molecular dynamics. In order to do the numerical integration, the Langevin equation can be written as

$$\mu\ddot{r}(t) = F(r(t)) - \gamma\mu\dot{r}(t) + \sqrt{2kT\gamma\mu}\eta(t), \quad (2.4.30)$$

where

$$\gamma = \zeta_0/\mu, \quad R(t) = \sqrt{2kT\gamma\mu}\eta(t) \quad (2.4.31)$$

The second term at the right side of the equation represents the friction kernel, where γ has a convolution integral form due to the fact that the bath requires a finite time to respond to any fluctuation in the motion of the system and that the force that the bath exerts on the system depends on the prior motion of the system. The last term is the noise term containing a delta function, denoted as η , to ensure that the force at a time t is uncorrelated with the force at any other time.

Similar to Verlet integrator, the solver for the Langevin equation can be written as

$$\begin{aligned} r(t + \Delta t) &= r(t) + \Delta t v(t) + A(t) \\ v(t + \Delta t) &= v(t) + \frac{1}{2}\Delta t [f(r(t + \Delta t)) + f(r(t))] \\ &\quad - \Delta t \gamma v(t) + \sigma \sqrt{\Delta t} \xi(t) - \gamma A(t). \end{aligned} \quad (2.4.32)$$

Here Δt is set as small time interval and

$$\begin{aligned} A(t) &= \frac{1}{2}\Delta t^2 (f(r(t)) - \gamma v(t)) + \sigma \Delta t^{3/2} \left(\frac{1}{2}\xi(t) + \frac{1}{2\sqrt{3}}\theta(t) \right) \\ \sigma &= \sqrt{2kT\gamma/\mu} \\ f(r) &= F(r)/\mu. \end{aligned}$$

It can be noted that the integrator in Eq.(2.4.32) will be reduced to the velocity Verlet integrator in Eq.(2.4.17, 2.4.16) when $\gamma = 0$ and $\sigma = 0$, which is the limit of no bath coupling.

The evaluation of the observable is necessary to provide an estimate of the thermodynamic expectation value within representative samples, resulting in the form

$$\langle A \rangle = \lim_{t_0 \rightarrow \infty} \frac{1}{t_0} \int_0^{t_0} dt A(\mathbf{R}(t), \mathbf{P}(t)). \quad (2.4.33)$$

Here, $A(\mathbf{R}(t), \mathbf{P}(t))$ denotes the instantaneous value of the observable A obtained for the phase-space configuration $\mathbf{R}(t), \mathbf{P}(t)$ evaluated with the full many-body Hamiltonian $H(\mathbf{R}, \mathbf{p})$.

Harmonic sampling provides a way to create samples under the harmonic approximation, starting from replacing the many-body potential shown in the left of Fig. (2.3) by

$$\mathcal{V}^{(2)}(\mathbf{R}) = \frac{1}{2} \sum_{I,J} u_I \cdot \Phi_{IJ} u_J, \quad (2.4.34)$$

where Φ_{IJ} denotes force constant matrices and u_I represents atomic displacements. Thus, Newton's equation of motion can be written as

$$\begin{pmatrix} M_1 \ddot{u}_1 \\ M_2 \ddot{u}_2 \\ \vdots \\ M_N \ddot{u}_N \end{pmatrix} = \begin{pmatrix} \Phi_{11} & \Phi_{12} & \cdots & \Phi_{1N} \\ \Phi_{21} & \Phi_{22} & \cdots & \Phi_{2N} \\ \vdots & \vdots & \ddots & \vdots \\ \Phi_{N1} & \Phi_{N2} & \cdots & \Phi_{NN} \end{pmatrix} \begin{pmatrix} u_1 \\ u_2 \\ \vdots \\ u_N \end{pmatrix} \quad (2.4.35)$$

The analytical solution to this equation can be expressed as

$$u_I(t) = \frac{1}{\sqrt{M_I}} \sum_s \mathbf{e}_{sI} A_s \sin(\omega_s t + \phi_s) \quad (2.4.36)$$

with the mass-reduced dynamical matrix

$$D_{IJ} = \Phi_{IJ} / \sqrt{M_I M_J}. \quad (2.4.37)$$

Here, \mathbf{e}_{sI} , s , ω_s denotes the eigenvector of the dynamical matrix corresponding to atom I , phonon mode and frequency respectively, which is similar to the expression in Sec. (2.3.1) related to the lattice dynamics model in harmonic approximation. The amplitudes A_s and phases ϕ_s are fixed by the initial condition $\mathbf{R}(t_0), \mathbf{P}(t_0)$. In thermal equilibrium, the average kinetic energy of each mode is $\frac{1}{2} k_B T$ and thus

$$\langle A_s \rangle = \sqrt{\frac{\hbar}{\omega_s} \left(n_s(\omega_s, T) + \frac{1}{2} \right)} \xrightarrow{k_B T \gg \hbar \omega_s} \frac{\sqrt{2 k_B T}}{\omega_s}. \quad (2.4.38)$$

If $A_s = \langle A_s \rangle$ for all s , the energy of each mode is exactly $k_B T$. However, in order to describe the thermal fluctuation implied by the sine equation in Eq. (2.4.36), a normally random distribution ζ_s is utilized[51]

$$\zeta_s = \int_0^{E_s} \frac{1}{k_B T} e^{-E/k_B T} dE. \quad (2.4.39)$$

with energy of each mode E_s . Therefore, in equilibrium at the temperature T , the harmonic Cartesian positions and velocities are

$$u_I = \sqrt{\frac{2k_B T}{M_I}} \sum_s \frac{1}{\omega_s} \sqrt{-\ln(1 - \zeta_s)} \cos(\omega_s t + \varphi_s) e_{sI} \quad (2.4.40)$$

and

$$\dot{u}_I = -\sqrt{\frac{2k_B T}{M_I}} \sum_s \sqrt{-\ln(1 - \zeta_s)} \sin(\omega_s t + \varphi_s) e_{Is}. \quad (2.4.41)$$

In practice, the force constants is a condensed representation in $(N_{\text{prim}}, N, 3, 3)$ shape, where N_{prim} is the number of atoms in the primitive cell and N is the number of atoms in the supercell. For creating samples, they need to be mapped to a full $(3N \times 3N)$ shape. This method can not only estimate the thermodynamic expectation values of the observables in interest by approximating the ensemble average but also contribute to pre-thermalizing the system in MD simulations given the distribution of displacements.

2.4.4. Anharmonicity

It has been mentioned in previous sections that the anharmonic lattice vibrations play pivotal roles in condensed matter, since they affect how the atoms interact and conduct heat, which can not be explained by the harmonic approximation.[52] The vibrational thermal transport can be assessed via either perturbation theory in Sec. (2.3.3) by expanding the potential energy to third or fourth order in the atomic displacements and solving phonon Boltzman transport equation(BTE), or *ab initio* Green-Kubo calculation which will be discussed in next section. In order to define the anharmonicity, the full potential in the many-body Hamiltonian within Born-Oppenheimer approximation defined in Eq. (2.4.1) can be split into two parts, one is for harmonic potential $\mathcal{V}^{(2)}$ and the second one is for all other anharmonic effects $\mathcal{V}^A(\mathbf{R})$. [53]

$$\mathcal{V}(\mathbf{R}) = \mathcal{V}^{(2)}(\mathbf{R}) + \mathcal{V}^A(\mathbf{R}). \quad (2.4.42)$$

In addition, the forces can therefore be split into harmonic and anharmonic contributions as well due to linearity of the differential when applied in Newton's equation.

$$\mathbf{F}_I = \mathbf{F}_I^{(2)} + \mathbf{F}_I^A \quad (2.4.43)$$

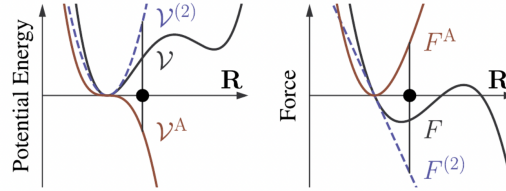


Figure 2.3.: Sketch of a one-dimensional potential-energy surface and the force, both with harmonic and anharmonic contributions. Fig. from Ref. [54]

The anharmonicity is measured in terms of the forces but not the potential energy since the force can be resolved into each atom to give a clear microscopic insight. For each configuration \mathbf{R} there will be $3N$ force components $(\mathbf{F}_1, \dots, \mathbf{F}_N)$. The anharmonicity is quantitatively measured by a so-called *anharmonicity score* σ^A defined as

$$\sigma^A(T) = \sqrt{\frac{\sum_{I,\alpha} \langle (F_{I,\alpha}^A)^2 \rangle_T}{\sum_{I,\alpha} \langle (F_{I,\alpha})^2 \rangle_T}}. \quad (2.4.44)$$

Here, $F_{I,\alpha}$ is the force obtained from *ab initio* MD on atom I along the a Cartesian direction α . $\langle \cdot \rangle_T$ represents thermodynamic averaging over a selected ensemble at temperature T . $F_{I,\alpha}^A$ is the anharmonic component of the atomic force, which is given by the difference between $F_{I,\alpha}$ and its harmonic component $F_{I,\alpha}^{(2)}$. Essentially, σ^A measures the standard deviation of the distribution of anharmonic force components $\sigma[F^A]_T$ at a given temperature normalized by the standard deviation of the actual force distribution $\sigma[F]_T$ via *ab initio* MD with $\sigma[F]_T$ being defined as

$$\sigma[F]_T = \sqrt{\frac{1}{3N} \sum_{I,\alpha} \langle F_{I,\alpha}^2 \rangle_T}. \quad (2.4.45)$$

In order to better elucidate the concepts and give a intuitive impression on the anharmonicity score, two prototypical materials are taken as an example. One is the well-known

harmonic material Si and the second one is an anharmonic perovskite material KCaF_3 . Both of them are sampled by *ab initio* molecular dynamics simulations at 300 K. The joint normalized distributions between total force F and anharmonic force F^A are shown in Fig. (2.4) which have been normalised by the standard deviation of DFT forces bounded between the horizontal dashed lines. The color saturation increases linearly from zero to the maximum value. It can be noticed that the distribution of anharmonic force components for the perovskite KCaF_3 is more than twice as broad as that for the silicon, indicated by the width of the horizontal dash lines. The anharmonicity score σ^A can be interpreted as the contributions of anharmonic forces to the total forces. In this sense, 36 % of the forces stem from anharmonic contributions in KCaF_3 , and 15% in silicon, with $\sigma_{\text{KCaF}_3}^A = 0.36$ and $\sigma_{\text{Si}}^A = 0.15$.

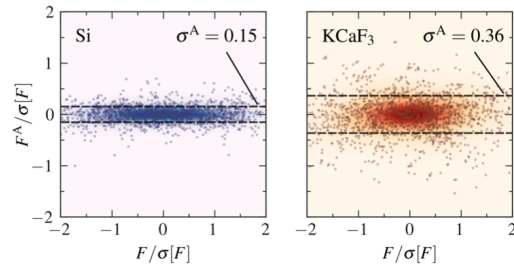


Figure 2.4.: Normalized anharmonic force components versus normalized force components. Dashed horizontal lines: Width of the distribution estimated from standard deviation. Individual dots are force components sampled during an *ab initio* MD simulations. Fig. from Ref. [54].

2.5. The Green-Kubo calculation method

The above discussion in Sec. (2.4.3) and Sec. (2.4.2) has been restricted to equilibrium ensembles, including microcanonical ensemble and canonical ensembles which are generated by coupling a physical system to a heat bath. The equilibrium ensembles allow a wide variety of thermodynamic and structural properties of systems to be computed. Apart from that, the linear response theory guarantees that some dynamic or transport properties for example, shear viscosity coefficients and thermal conductivity, can also be calculated without a time-dependent perturbation.

2.5.1. Linear response theory

The goal of response theory is to figure out how a system reacts to external influences, for instance, applied electric and magnetic fields which are time-dependent. This response can be described by the expectation value of a phase-space observable in a system characterized by the many-body Hamiltonian $\mathcal{H}^0(\Gamma)$ in company with an external perturbation $\mathcal{H}'(\Gamma, t)$ so as

$$\mathcal{H}(\Gamma, t) = \mathcal{H}^0(\Gamma) + \mathcal{H}'(\Gamma, t). \quad (2.5.1)$$

with the perturbation

$$\mathcal{H}'(\Gamma, t) = A(\Gamma)F(t) \quad (2.5.2)$$

Here, $A(\Gamma)$ is an operator which now represents the observables of the system, and $F(t)$ is an explicitly time-dependent force function, i.e. *sources*. Now, we will take a look at a general class of driven classical systems and their corresponding phase space distributions. Consider a classical system described by $3N$ generalized coordinates q_i and their conjugate generalized momenta p_i , where the weak driving force is assumed as small perturbation to the system. The Hamiltonian's equations of motion for the system is

$$\begin{aligned} \dot{q}_i &= \frac{\partial \mathcal{H}}{\partial p_i} + C_i(q, p)F_e(t) \\ \dot{p}_i &= -\frac{\partial \mathcal{H}}{\partial q_i} + D_i(q, p)F_e(t), \end{aligned} \quad (2.5.3)$$

where $C_i(q, p)$ and $D_i(q, p)$ are phase space functions determined by the particular external perturbation. In addition, the Hamiltonian's equations of motion is imposed to satisfy the

incompressibility condition

$$\sum_{i=1}^{3N} \left[\frac{\partial \dot{q}_i}{\partial q_i} + \frac{\partial \dot{p}_i}{\partial p_i} \right] = 0. \quad (2.5.4)$$

Substituting Eq. (2.5.3) into Eq. (2.5.4) leads to a restriction on the choice of the phase space functions

$$\sum_{i=1}^{3N} \left[\frac{\partial C_i}{\partial q_i} + \frac{\partial D_i}{\partial p_i} \right] = 0. \quad (2.5.5)$$

In addition, when the equations of motion have zero phase space compressibility, the phase space distribution function $f(x, t)$ satisfies the Liouville equation

$$\frac{\partial}{\partial t} f(x, t) + iL f(x, t) = 0, \quad iL = \dot{x} \cdot \nabla_x \quad (2.5.6)$$

where iL is the Liouville operator. When the external perturbation is small, we assume that the solution $f(x, t)$ can be written in the form

$$f(x, t) = f_0(\mathcal{H}(x)) + \Delta f(x, t). \quad (2.5.7)$$

Here the Hamiltonian $\mathcal{H}(x)$ is equal to $\mathcal{H}(p, q)$ and $f_0(\mathcal{H}(x))$ is the equilibrium phase space distribution function generated by the corresponding unperturbed system ($C_i = D_i = 0$) so that it satisfy the equilibrium Liouville equation

$$iL_0 f_0(\mathcal{H}(x)) = 0, \quad (2.5.8)$$

where iL_0 is the unperturbed Liouville operator. Note that the Liouville operator can also be written as a perturbation form

$$iL = \dot{x} \cdot \nabla_x = (\dot{x}_0 + \Delta \dot{x}(t)) \cdot \nabla_x = iL_0 + i\Delta L(t). \quad (2.5.9)$$

Thus, the Liouville equation becomes

$$\frac{\partial}{\partial t} (f_0(\mathcal{H}(x)) + \Delta f(x, t)) + (iL_0 + i\Delta L(t)) (f_0(\mathcal{H}(x)) + \Delta f(x, t)) = 0. \quad (2.5.10)$$

In the above equation, the second order term $i\Delta L \Delta f(x, t)$ is neglected if driving force terms in Eq. (2.5.3) constitute a small perturbation. This approximation is the core of *linear response theory*. Within linear response theory, the Liouville equation Eq. (2.5.10) is reduced to

$$\left(\frac{\partial}{\partial t} + iL_0 \right) \Delta f(x, t) = -i\Delta L(t) f_0(\mathcal{H}(x)). \quad (2.5.11)$$

It is a simple first order inhomogeneous differential equation that can be solved using the unperturbed classical propagator $\exp^{iL_0 t}$ as an integrating factor. Using the normalization condition as an ansatz

$$\int dx f(x, t) = 1, \quad (2.5.12)$$

gives the ensemble average of any function $a(x)$, expressed as

$$\begin{aligned} \langle a \rangle_t &= \int dx a(x) f(x, t) \\ &= \int dx a(x) f_0(\mathcal{H}(x)) + \int dx a(x) \Delta f(x, t) \\ &= \langle a \rangle + \int dx a(x) \Delta f(x, t) \\ &= A(t). \end{aligned} \quad (2.5.13)$$

Here, $\langle a \rangle_t$ is the average of $a(x)$ in the unperturbed ensemble described by $f_0(H(x))$, and the notation $A(t) = \langle a \rangle_t$ indicates an average in the nonequilibrium ensemble corresponding to the time-dependent property $A(t)$.

$$A(t) = \langle a \rangle - \beta \int_0^t ds F_e(s) \int dx f_0(\mathcal{H}(x)) a(x_{t-s}) j(x), \quad (2.5.14)$$

where $j(x)$ is the dissipative flux

$$j(x) = - \sum_{i=1}^{3N} \left[D_i(x) \frac{\partial \mathcal{H}}{\partial p_i} + C_i(x) \frac{\partial \mathcal{H}}{\partial q_i} \right] \quad (2.5.15)$$

In the second term in Eq. (2.5.14), it shows that the Hamilton's equations of motion evolves from each initial point x with phase space function $a(x)$ to new phase space point x_{t-s} with $a(x_{t-s})$. Then an average of $a(x_{t-s}) j(x)$ is taken over the phase space with respect to the unperturbed distribution function $f_0(\mathcal{H}(x))$ of all possible initial conditions. Finally, we integrate the result multiplied by $F_e(s)$ over s from 0 to t , which results in the equilibrium time correlation function

$$\int dx f_0(\mathcal{H}(x)) a(x_{t-s}) j(x) \equiv \langle a(t-s) j(0) \rangle, \quad (2.5.16)$$

with the right hand side as a commonly used notation for a time correlation function, which in turn gives a more compact form of Eq. (2.5.14)

$$A(t) = \langle a \rangle_t = \langle a \rangle - \beta \int_0^t ds F_e(s) \langle a(t-s) j(0) \rangle \quad (2.5.17)$$

2.5.2. Equilibrium time correlation functions

The equilibrium time correlation function $C_{AB}(t)$ between two observables A and B is defined as

$$\begin{aligned} C_{AB}(t) &= \langle a(0)b(t) \rangle = \int dx f(x) a(x) e^{iLt} b(x) \\ &= \int dx f(x) a(x) b(x_t(x)), \end{aligned} \quad (2.5.18)$$

corresponding to phase space functions $a(x)$ and $b(x)$, with respect to a normalized equilibrium distribution function $f(x)$ and dynamics generated by a Liouville operator iL . It can be inspected that e^{iLt} can act as either to the right as a forward propagator or to the left as a backward propagator, and thus

$$\langle A(0)B(t) \rangle = \langle A(-t)B(0) \rangle. \quad (2.5.19)$$

At the initial condition, i.e. $t=0$,

$$C_{AB}(0) = \langle AB \rangle = \int dx f(x) a(x) b(x). \quad (2.5.20)$$

The influence of each initial condition on the resultant trajectories generated by e^{iLt} rapidly becomes negligible as time proceeds, which means there is a characteristic time, called the *correlation time*, over which the trajectory $x_t(x)$ appears to be particular to a given choice of x and beyond which $x_t(x)$ is essentially indistinguishable from any other trajectory.

In order to see what the existence of a correlation time implies for a correlation function, consider the special case $a(x) = b(x)$. The time correlation function turns to be the so-called *autocorrelation function*

$$C_{AA}(t) = \langle a(0)a(t) \rangle = \int dx f(x) a(x) a(x_t(x)). \quad (2.5.21)$$

For very short times, $a(x_t(x))$ and $a(x)$ are not very different, hence they are highly correlated while for times longer than the correlation time, the trajectory loses memory of its initial condition, and $a(x_t(x))$ and $a(x)$ become uncorrelated.

2.5.3. Heat flux autocorrelation function

Equilibrium molecular dynamics (EMD) calculations are performed using Green-Kubo formalism which relates transport quantities to the duration of fluctuations in a microscopic state of the system. The underlying principle is *fluctuation-dissipation theorem* which consider the small local fluctuations dissipation as the material's feedback to a stimulus. Mathematically this is achieved by integrating the current autocorrelation function,

$$\kappa = \frac{V}{3k_B T^2} \int_0^\infty \langle \mathbf{J}(t) \mathbf{J}(t + \tau) \rangle d\tau \quad (2.5.22)$$

where k_B is Boltzmann constant, T is the temperature, V is the volume of the simulated region, J is the current that drives transport property κ . $\langle \mathbf{J}(t) \mathbf{J}(t + \tau) \rangle$ is the non-normalized heat current autocorrelation function(HCACF). Although the equilibrium molecular dynamics approach suffers from size artifacts, the use of periodic boundary conditions in EMD allows for a smaller system size. Even so, fully converging the autocorrelation function requires very long simulation time and often a compromise has to be made between including the contribution of slow processes and introducing a random error. To accelerate this process, a cutoff time t_c is chosen to avoid integrating parts of the autocorrelation function after it has effectively decayed, which in turn introduce the noises.

The oscillatory behavior of the autocorrelation function(ACF) can be observed for a system in equilibrium, where the average current of any property is zero, and the ACF is expected to decay to zero given sufficient time. In addition, the integral of ACF contains large oscillations which is shown in Fig.(2.5) where an example of decaying HCACFs is take from graphite and the curves that rise to a plateau are integrals. The rapid decay corresponds to the contribution from short wavelength phonons to thermal conductivity, while the slower decay corresponds to the dominant contribution to thermal conductivity from long wavelength phonons.[55]

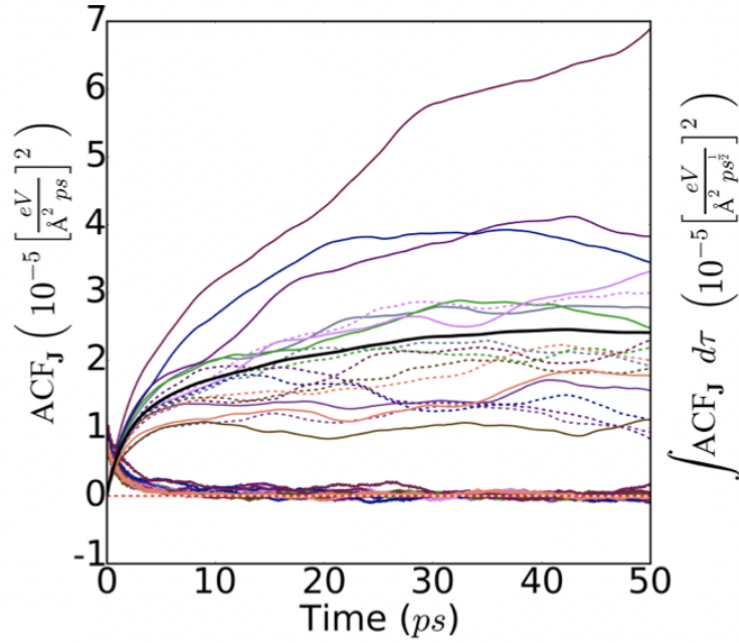


Figure 2.5.: HCAFs plotted along side their integrals computed from nine separate trajectories for perfectly crystalline, and periodically contiguous block of graphite with 10648 atoms. Fig. from Ref.[56]

2.5.4. Heat flux

In this part, the heat flux expression as a microscopic dynamical variable is derived step by step. First, a general microscopic dynamical variable and its spatial Fourier components are defined respectively as

$$A(\mathbf{r}, t) = \sum_{i=1}^N a_i(t) \delta[\mathbf{r} - \mathbf{r}_i(t)], \quad (2.5.23)$$

$$A_{\mathbf{k}}(t) = \int A(\mathbf{r}, t) \exp(-i\mathbf{k} \cdot \mathbf{r}) d\mathbf{r} = \sum_{i=1}^N a_i(t) \exp[-i\mathbf{k} \cdot \mathbf{r}_i(t)]. \quad (2.5.24)$$

Here, the $a_i(t)$ is some physical quantity such as the mass, velocity or energy of particle i and \mathbf{r}_i the time-dependent particle coordinate. A *conserved* microscopic dynamical variable

satisfies a continuity equation, so that

$$\frac{\partial A(\mathbf{r}, t)}{\partial t} + \nabla \cdot \mathbf{j}^A(\mathbf{r}, t) = 0 \quad (2.5.25)$$

where \mathbf{j}^A is the current associated with the variable A. Similarly, the corresponding continuity equation for the Fourier components of A is

$$\frac{\partial A_{\mathbf{k}}(t)}{\partial t} + i\mathbf{k} \cdot \mathbf{j}_{\mathbf{k}}^A(t) = 0, \quad (2.5.26)$$

which shows that spontaneous fluctuations in a conserved variable decay very slowly at long wavelengths. The time-dependent, microscopic particle density corresponds to the case when $a_i = 1$, i.e. a conserved local variable, written as

$$\rho(\mathbf{r}, t) = \sum_{i=1}^N \delta[\mathbf{r} - \mathbf{r}_i(t)]. \quad (2.5.27)$$

Then the associated particle current is

$$\mathbf{j}(\mathbf{r}, t) = \sum_{i=1}^N \dot{\mathbf{r}}_i(t) \delta[\mathbf{r} - \mathbf{r}_i(t)], \quad (2.5.28)$$

with Fourier component

$$\mathbf{j}_{\mathbf{k}}(t) = \sum_{i=1}^N \dot{\mathbf{r}}_i(t) \exp[-i\mathbf{k} \cdot \mathbf{r}_i(t)]. \quad (2.5.29)$$

Each Fourier component may be separated into longitudinal (\mathbf{j}_{\parallel}) and transverse (\mathbf{j}_{\perp}) parts, the two parts being parallel and perpendicular, respectively, to the wavevector \mathbf{k} .

Now the total energy of the system \mathbf{E} and its associated energy density \mathbf{e} are taken as an example for the microscopic dynamical variable. Firstly the energy density satisfies the continuity equation as

$$\dot{\mathbf{e}}(\mathbf{r}) = -\nabla \cdot \mathbf{j}(\mathbf{r}), \quad (2.5.30)$$

and its Fourier component will be

$$\dot{\mathbf{e}}(\mathbf{k}) = -i\mathbf{k} \cdot \mathbf{j}(\mathbf{k}). \quad (2.5.31)$$

Multiplying the Eq. (2.5.31) by $i\mathbf{k}$ in both sides and considering the orthogonality of \mathbf{j} lead to the expression for the longitudinal current

$$\mathbf{j}_{\parallel}(\mathbf{q}) = i\frac{\mathbf{q}}{q^2}\dot{e}(\mathbf{q}). \quad (2.5.32)$$

The spatially average over the above longitudinal current with $\frac{1}{V}\int_V d^3r$ results in the heat flux

$$J = \frac{1}{V}\int d^3r\mathbf{j}_{\parallel}(\mathbf{r}). \quad (2.5.33)$$

Finally the heat flux is given as the time derivative of the energy density

$$J(t) = \frac{1}{V}\int d^3r\mathbf{r}\dot{e}(\mathbf{r}, t), \quad (2.5.34)$$

since the integral over the infinite volume in real space equals to the long wavelength limit of the current in reciprocal space. If the energy density relies on each atomic contribution, it can be then expressed as

$$e(\mathbf{r}, t) = \sum_I E_I(t)\delta(\mathbf{r} - \mathbf{R}_I(t)), \quad (2.5.35)$$

followed by the heat flux

$$\mathbf{J}(t) = \frac{1}{V}\frac{d}{dt}\sum_I E_I(t)\mathbf{R}_I(t) = \frac{1}{V}\sum_I \dot{E}_I(t)\mathbf{R}_I(t) + \frac{1}{V}\sum_I E_I(t)\dot{\mathbf{R}}_I(t). \quad (2.5.36)$$

Here the last equation means that the heat flux can be split into two parts, namely the *virial* or *kinetic* current and the *convective* or *potential* current.[57] Typically the contributions from convection can be neglected in solids due to the results shown in the work by *Kinaci et. al*[58] that the heat current considering only the potential current(black solid lines) presents nearly the same result with the one includes kinetic and potential contribution. In fact, the convection contribution to thermal conductivity is much lower compared to the virial flux in a bulk non-convective solid.[59] This result can be partly explained intuitively that the intermolecular forces in solids are strong to hold the molecular at fixed position and there is no relative motion between the molecules while the convection current requires the movement of the molecules either by external force or by density differences. However, this convective current term dominates in liquid or gas situation, where diffusion directly contributes to the convective heat flux.[55]

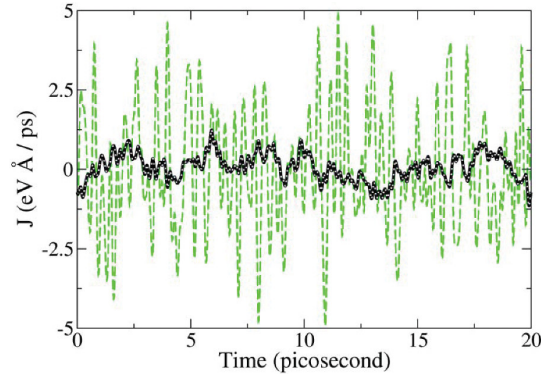


Figure 2.6.: Heat current obtained from analytical, (black) solid line, and numerical, (green) dashed line, results from non-convective solid. (Grey) Dotted line represents numerical result from the combination of convective and virial contributions. Fig. from Ref. [58]

2.5.5. Thermal conductivity via *ab initio* Green-Kubo calculation

Thermal conductivity describes the capability of a material to conduct heat. When a temperature gradient $\nabla T(\mathbf{R})$ is present, a heat flux spontaneously develops to move the system back toward thermodynamic equilibrium. This dynamic process is described by Fourier's law

$$J(\mathbf{R}) = -\kappa(T, p) \cdot \nabla T(\mathbf{R}) \quad (2.5.37)$$

The vibrational motion of the atoms, i.e. phonons, mostly contributes to the thermal conductivity in insulators and semiconductors. The transport coefficient can also be expressed by *Green-Kubo relation* in terms of the integral of an equilibrium time correlation function, which can be easily computed within a molecular dynamics simulation.[60] The thermal conductivity tensor at temperature T can be calculated by means of Green-Kubo calculation as an ensemble average, shown as

$$\kappa^{\alpha\beta}(T) = \int d\Gamma \kappa^{\alpha\beta}(\Gamma) f_T(\Gamma), \quad (2.5.38)$$

where the statistical weight for canonical ensemble is given by the Boltzmann factor

$$f_T(\Gamma) = \frac{1}{\mathcal{Z}} e^{-\frac{1}{k_B T} \mathcal{H}(\Gamma)}. \quad (2.5.39)$$

Here Γ represents phase space configurations and α, β denote the Cartesian components of the tensor. In order to evaluate the thermal conductivity tensor in finite simulations

the integrals need to be discretized and truncated to finite domains and some start configurations Γ_0^i from above NVT calculations are picked up.

$$\kappa^{\alpha\beta}(T) \approx \frac{1}{M} \sum_{i=1}^M \kappa^{\alpha\beta}(\Gamma_0^i) \quad (2.5.40)$$

Then the NVE MD calculation generates the trajectory Γ_t^i and the heat flux $J^\alpha(\Gamma_t^i)$ for each start configuration. After computing the thermal conductivity for each trajectory, the final value is given by the mean of the individual trajectories indicated in Eq. (2.5.40). The statistical error due to the finite ensemble average is estimated by the standard deviation of the mean

$$\Delta\kappa^{\alpha\beta}(T) = \frac{1}{\sqrt{N}} \sqrt{\frac{1}{N} \sum_i (\kappa^{\alpha\beta}(T) - \kappa^{\alpha\beta}(\Gamma_0^i))^2}. \quad (2.5.41)$$

3. Toy model calculation

To better explain and exemplify the various steps in a Green-Kubo calculation, the one-dimensional CH_2 chain, shown in Fig. (3.1), is chosen as toy model. We emphasize that these are purely pedagogical calculations that do not aim at realistic predictions, since such an infinite 1D CH_2 chain hardly exists in reality. In a first step, we calculate its phonon band structure and anharmonicity. The structure is studied at the LDA level of theory using the *Perdew-Wang LDA* functional and light-default basis set in the all-electron, full potential code *FHI-aims*[20]. The supercell size is $(1 \times 1 \times 2)$, containing 12 atoms. The starting structure is given by the space group $\text{Pmma}(51)$ with the lattice constant 3\AA . The MD simulations are performed via *FHI-vibes*[21, 22]. Firstly, the k grid and basis set convergence in the DFT calculations for electrons are inspected, where a denser grid leads to a more resolved band structure at the expenses of the increasing computational cost compared with a coarser grid. As it is discussed in Sec. (2.2.4), the basis set, including light, intermediate and so on, controls how the initial radial functions are chosen to do the calculation. Then the phonon bandstructure and its convergence on the supercell size are inspected with the *phonopy* package[14]. In addition, its anharmonicity is calculated by molecular dynamics(MD) using the anharmonicity introduced in Sec.(2.4.4) . Finally, the thermal conductivity is determined by the *Green-Kubo* method and the *phono3py* package[40], respectively.

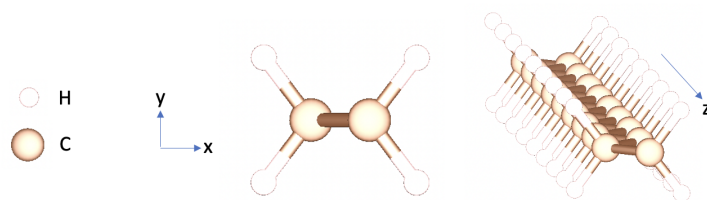


Figure 3.1.: Crystal structure of the fictitious one dimensional CH_2 chain projected onto the xy plane(middle) where the z coordinate is along the chain(right).

3.1. Relaxation

Since the structure is a one dimensional chain, only the lattice vector along the chain, here in z direction can change. In this case, the relaxation is constrained accordingly. The BFGS optimization is performed utilizing the functional *pw-lda* until forces and stresses are converged below $1 \text{ meV}/\text{\AA}$. After the energy converged in the relaxation, the structure is still in the space group Pmma(51) but the new lattice constants turns to be 2.526 \AA for the lattice.

Energy convergency with basis set and k grid

As discussed in Sec. (2.2.4), the basis set is related to the how the Kohn-Sham eigenfunctions are expanded in terms of numeric atom-centered orbitals(NAO). In addition, the integration of periodic functions over the entire Brillouin zone(BZ) can be replaced by the calculation at a selected set of points in BZ, i.e, a k grid, which significantly saves computational effort. It was presented by Monkhorst and Pack[61] that a rectangular grid with the form $(M_x \times M_y \times M_z)$ can be used to sample the Brillouin zone. The choice of both the basis set and the k grid mesh relies on the convergence of the desired quantity to be predicted or calculated. In this CH_2 -case, the k grid mesh only needs to cover the z direction since we are dealing with a one dimensional periodicity.

From the below Fig. (3.2), the final energy is slightly lower for both light and intermediate basis for all k grids, which means the light basis set is already enough to achieve *meV*-level total energy convergence. In addition, both the energy and lattice constant qualitatively converge with k grid $(1 \times 1 \times 4)$. Thus, for the following phonon calculation, the k grid $(1 \times 1 \times 4)$ will be inspected at first.

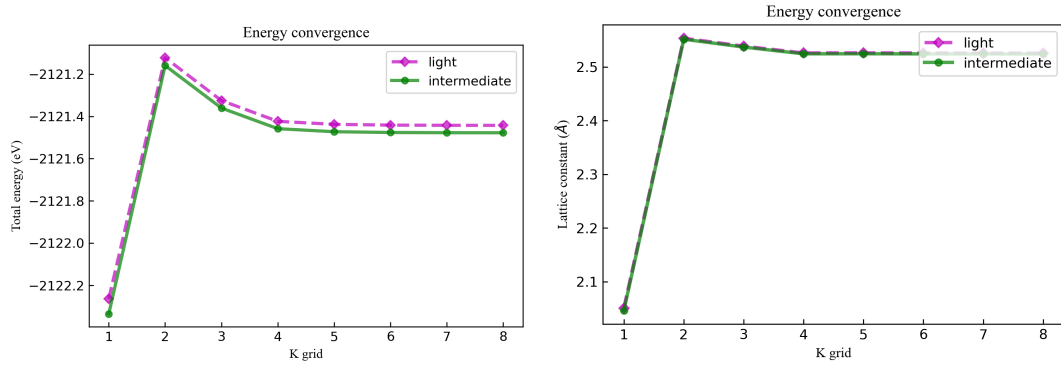


Figure 3.2.: Energy and lattice constant convergence with k grid and basis set for a one dimensional CH₂ chain.

3.2. Phonon calculation

The accurately relaxed structure obtained from the previous geometry optimization will be used for the phonon calculations. As shown in section 2.3.1, the displacement around the equilibrium position and the supercell size affects the solutions to the equation of motion shown in Eq. (2.3.6) and the phonon spectrum. When computing the real-space dynamical matrix, a supercell is first constructed by repeating the unit cell with an integer multiple along the directions of the primitive lattice vectors. Second, the finite-difference derivative is performed via

$$\begin{aligned}
 D_{I\mu J\nu} &= \frac{1}{\sqrt{M_I M_J}} \frac{\partial^2 E_{\text{tot}}(\mathbf{R})}{\partial \mathbf{u}_{I\nu} \partial \mathbf{u}_{J\mu}} \\
 &\approx \frac{1}{\sqrt{M_I M_J}} \frac{F_{J\mu}(+\Delta \mathbf{u}_{I\nu}) - F_{J\mu}(-\Delta \mathbf{u}_{I\nu})}{2\Delta \mathbf{u}_{I\nu}}.
 \end{aligned} \tag{3.2.1}$$

To this end, one calculates the forces in the entire supercell, while only displacing the atoms in the central unit cell. As schematically shown in Fig. (3.3), in which a unit cell is repeated 5 times horizontally and vertically, the forces can be expected to become zero outside a certain range (ellipsoidal area). This is where supercell convergence is achieved.

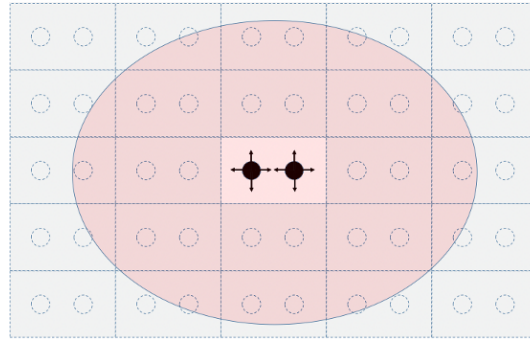


Figure 3.3.: Schematic illustration of the supercell method. Fig from Ref. [62]

Apart from the supercell size, another important numerical setting often called displacement $\Delta \mathbf{u}$ needs to be considered. In Sec. (2.3), under the harmonic approximation, the atomic nucleus is displaced within a short range around its equilibrium, which means the displacement should not be too high. This setting is controlled in *FHI-vibes* by the parameter "displacement". The phonon band structure is shown in Fig. (3.4) where the right figure represents a smaller displacement compared to the left one, while other numerical settings remain the same. The resulted phonon band structure shows that the calculation has already converged with the supercell $(1 \times 1 \times 2)$. There are four lines starting from Γ and each line represent a degree of freedom. In this case there are four acoustic modes corresponding to the translation in x, y, z axis and one molecular rotation, respectively. The zero frequency means that the excitation does not consume energy and the tiny negative frequency around the Γ point in the left figure means that the eigenvalue in Eq. (2.3.6) is imaginary and pictorially, there exists an energy saddle point. Since only the z axis periodicity is kept, the molecular can also rotate around the z axis without costing energy and this rotation is exactly the source of the fourth zero frequency at Γ . Although a smaller displacement corrects the saddle point, i.e. negative frequency, $\Delta \mathbf{u}$ needs to be large enough so that the finite difference in Eq. (3.2.1) is not dominated by numerical noise.

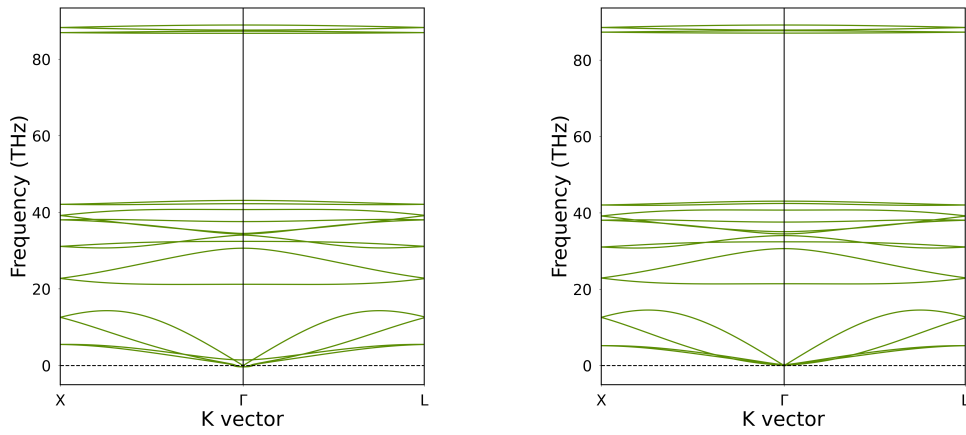


Figure 3.4.: The phonon band structures with displacement 0.01(left) and 0.001(right) for the C_2H_4 chain.

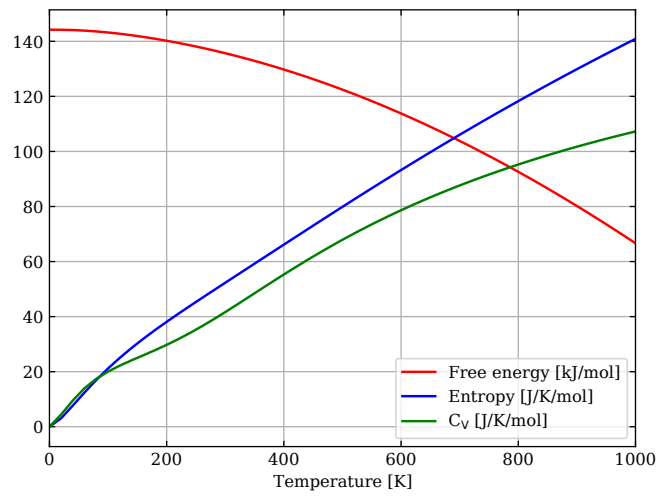


Figure 3.5.: Free energy and entropy of CH_2 and the respective specific heat C_v computed in the harmonic approximation .

3.2.1. Thermal conductivity by lattice dynamics method

The thermal conductivity calculation using the lattice dynamics method is implemented in the *phono3py* package[40]. It determines the third order force constants via

$$\Psi_{IJK}^{\alpha\beta\gamma} = \frac{\partial^3 E}{\partial R_I^\alpha \partial R_J^\beta \partial R_K^\gamma} = \frac{\partial^2 F_I^\alpha}{\partial R_J^\beta \partial R_K^\gamma} = \frac{\partial \Phi_{IJ}^{\alpha\beta}}{\partial R_K^\gamma} \approx \frac{\Phi_{IJ}^{\alpha\beta}(\delta R_K^\gamma) - \Phi_{IJ}^{\alpha\beta}}{\delta R_K^\gamma}, \quad (3.2.2)$$

by a *finite difference approach*. As in the previous phonon calculation, a $(1 \times 1 \times 2)$ supercell was used to compute the third order constant and then a $(45 \times 45 \times 45)$ \mathbf{q} mesh was used to compute the Fourier transformed third order force constant defined in Eq. (2.3.22). The imaginary part of the self-energy Γ_s and phonon lifetime τ can be subsequently obtained by Eq. (2.3.23, 2.3.25). Eventually, the diagonal entries of the lattice thermal conductivity tensor can be calculated by Eq. (2.3.26)

$$\kappa = \frac{1}{NV_0} \sum_s C_s \mathbf{v}_s \otimes \mathbf{v}_s \tau_s^{\text{SMRT}}, \quad (3.2.3)$$

with the phonon group velocity \mathbf{v}_s and the specific heat capacity C_s conveniently calculated by Eq.(2.3.28) and Eq. (2.3.29) in the previous phonon calculations. Due to the one dimensional structure of our CH_2 model, diagonal entries of the thermal conductivity tensor are reduced to only one component, i.e. $\kappa = \kappa_{zz}$. The result is given in Fig. (3.6) showing that κ decreases dramatically between 100K and 150K and then saturates at 250K with the value 0.661 W/mK . Additionally, in molecular crystals with the presence of many H atoms, Bose-Einstein statistics, and particularly zero-point motion, should be specifically accounted for. In this work, nuclear quantum effects of the atoms are rigorously incorporated into the calculation by the Bose-Einstein distribution (Eq. (2.3.22)).

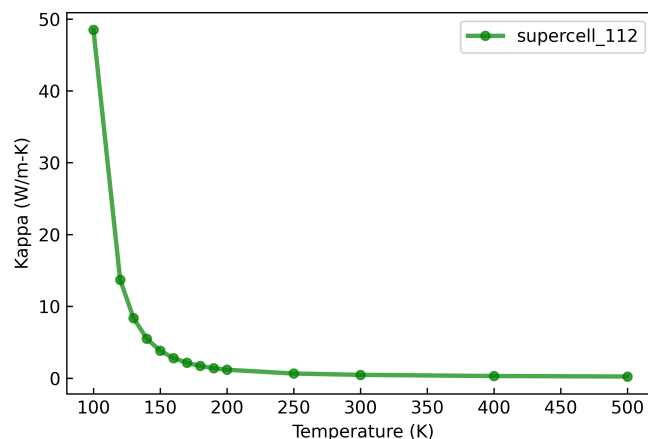


Figure 3.6.: Thermal conductivity calculated with a supercell (1x1x2) for C_2H_4 .

3.3. Molecular dynamic calculation

In order to calculate the thermal conductivity by the Green-Kubo method described in Sec. (2.5.5), the trajectory has to be created within NVT ensemble generated by a Langevin thermostat starting from some initial configuration. This step is called thermalization. In this step, a simulation at non-constant energy is performed by coupling the system to a thermal bath which must be incorporated explicitly into the Langevin equation. The Langevin equation features perturbation of the nuclei induced by a velocity-dependent friction γ , and a stochastic force proportional to a white-noise kernel $\eta(t)$, shown in Eq. (2.4.30). In this part, the effects of friction parameter and temperature on the displacement are inspected. The maximum trajectory length is set to 10 picoseconds and each time step is 1 femtosecond which is reasonable short for this light system.

The time evolution of the temperature at 200K with the friction parameter 0.02 is shown in Fig. (3.7), where the pre-thermalization occurs in the first 1000 time steps. Besides, the time evolution of displacement at 200K with 4 different friction parameters is given in Fig. (3.8). It can be noted that there exist some periodicity in the displacement, which reflects the rotation motion of the molecular chain. In addition, a larger friction parameter

breaks the periodicity with more zigzag features and generally lowers the displacement, i.e, damps the motion.

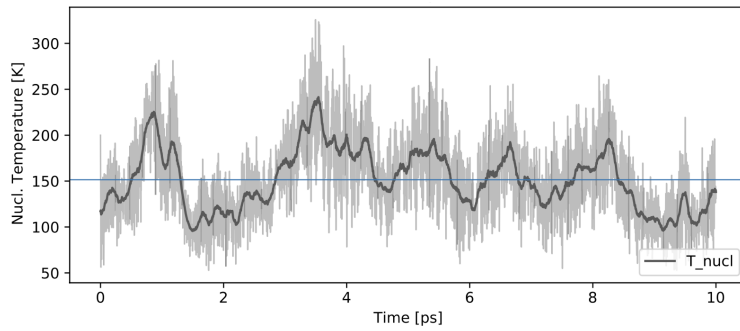


Figure 3.7.: Temperature evolution of C_2H_4 with friction parameter 0.02 and a target temperature of 200K.

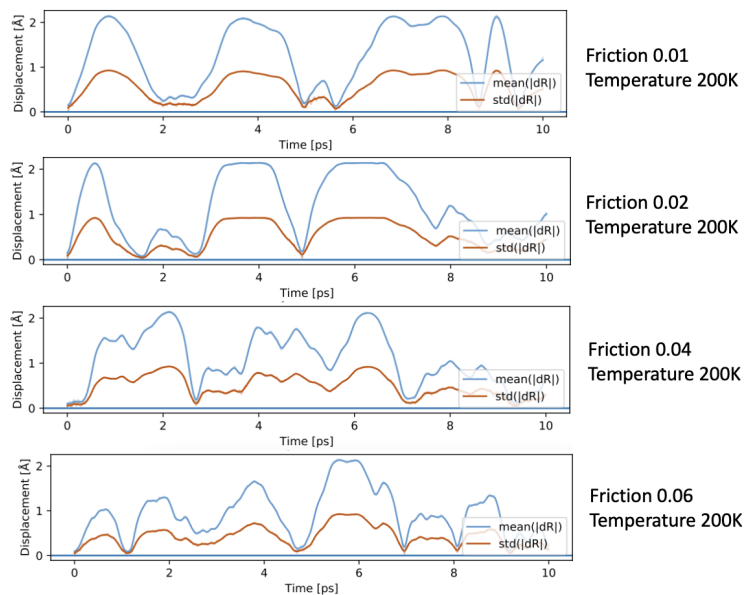


Figure 3.8.: Displacement evolution of C_2H_4 with friction parameter 0.01, 0.02, 0.04 and 0.06 at a target temperature of 200K.

The time evolution governed by Langevin equation is inspected again with various target

temperature, namely, 50K, 100K, 200K, 300K. The results are shown in Fig. (3.9) and indicate that when the friction parameter is increased to a even higher value 0.3, the zigzag feature is already pronounced in low temperature 50K and 100K and the displacement periodicity increases from 2 picosecond above to 10 picosecond. This phenomenon has a good agreement with what it implies in the above Langevin equation that larger friction parameter represents longer time for a system to react to the force. Interestingly, when the temperature is increased to 300K, the displacement does not go back to zero point, which hints at the fact that the C_2H_4 chain starts decomposing at 300K.

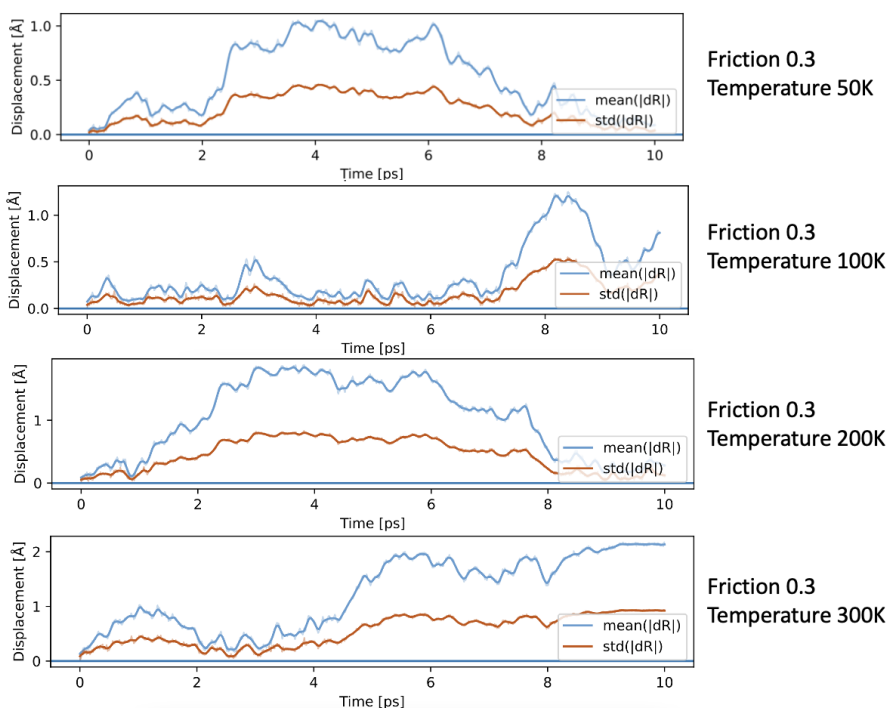


Figure 3.9.: Displacement evolution at temperature 50K, 100K, 200K and 300K with friction parameter 0.3.

3.3.1. Anharmonicity quantification

As discussed in Sec. (2.4.4), the anharmonic contribution to the potential energy $\mathcal{V}(\mathbf{R})$ is defined as

$$\mathcal{V}^A(\mathbf{R}) \equiv \mathcal{V}(\mathbf{R}) - \mathcal{V}^{(2)}(\mathbf{R}) \quad (3.3.1)$$

where the harmonic contribution at a given atomic configuration is

$$\mathcal{V}^{(2)}(\mathbf{R} = \mathbf{R}^0 + \Delta\mathbf{R}) = \frac{1}{2} \sum_{I,J} \Phi_{\alpha,\beta}^{I,J} \Delta R_I^\alpha \Delta R_J^\beta. \quad (3.3.2)$$

The harmonic force constants $\Phi_{\alpha,\beta}^{I,J}$ are obtained at the equilibrium configuration \mathbf{R}^0 . In practice, this force constant is provided by the phonon calculation in Sec. (3.2).

$$\Phi_{\alpha,\beta}^{I,J} = \left. \frac{\partial^2 \mathcal{V}}{\partial R_I^\alpha \partial R_J^\beta} \right|_{\mathbf{R}^0} \quad (3.3.3)$$

Similarly, the anharmonic contribution $F_{I,\alpha}^A(\mathbf{R})$ to the force components $F_{I,\alpha}(\mathbf{R})$ is defined as

$$F_{I,\alpha}^A(\mathbf{R}) = F_{I,\alpha}(\mathbf{R}) - F_{I,\alpha}^{(2)}(\mathbf{R}), \text{ with} \quad (3.3.4)$$

$$F_{I,\alpha}^{(2)} = - \sum_{J,\beta} \Phi_{\alpha,\beta}^{I,J} \Delta R_J^\beta.$$

In order to estimate the strength of anharmonic effects in a material, the anharmonicity score can be measured by

$$\sigma^A(T) \equiv \frac{\sigma[F^A]_T}{\sigma[F]_T} = \sqrt{\frac{\sum_{I,\alpha} \langle (F_{I,\alpha}^A)^2 \rangle_T}{\sum_{I,\alpha} \langle (F_{I,\alpha})^2 \rangle_T}}, \quad (3.3.5)$$

where $\langle \cdot \rangle_T$ represents the expectation value of a thermodynamics property at a given temperature T:

$$\langle O \rangle = \lim_{N_t \rightarrow \infty} \frac{1}{N_t} \sum_n^{N_t} (t_n). \quad (3.3.6)$$

Here, we clarify again that the $F_{I,\alpha}(t) \equiv F_{I,\alpha}[\mathbf{R}(t)]$ is the force component α on atom I at time t. The force components $F_{I,\alpha}(\mathbf{R})$ together with its anharmonic contributions $F_{I,\alpha}^A$ are calculated by Eq. (3.3.4) via an MD simulation. The anharmonicity scores at different temperature, namely 50K, 100K and 200K are given in the left panel of Fig. (3.10). It can be noted that the anharmonicity score is much higher than 1. However since this structure is not physical and just a theoretical model, one should not be too shocked by this results. In addition, the time dependence of the anharmonicity score is checked in the right panel by truncating down every trajectory at 100K to a length of 10 ps, indicating that 40 ps maximum time step has already given a converged results.

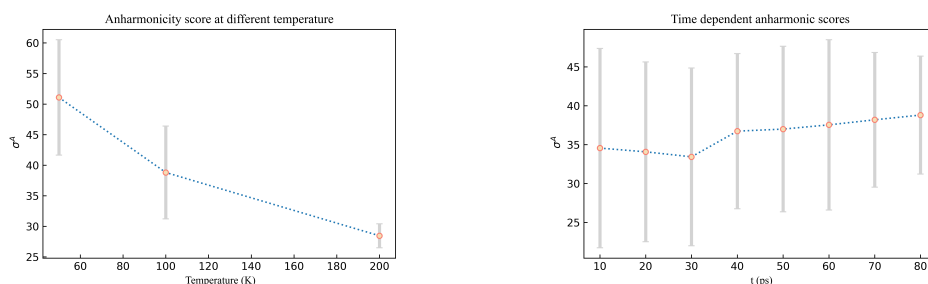


Figure 3.10.: σ^A as a function of temperature obtained from MD simulations.

3.4. Heat conductivity

3.4.1. Heat flux autocorrelation function

The calculation of thermal conductivity via Green-Kubo method relies on the heat flux autocorrelation function (HFACF) as it is discussed in Sec. (2.5.3) and Sec. (2.5.5). There is no average heat flux for a system in equilibrium, which means the Heat flux autocorrelation function (HCACF), i.e. the term inside the integral in Eq. (2.5.22), is therefore expected to decay to zero given sufficient time. The HCACF is crucial in computing thermal conductivity using the Green-Kubo method discussed in Sec. (2.5.3) and Sec. (2.5.5). In this part, HCACF is computed as the simulation progresses along x, y and z respectively, for the crystalline ($1 \times 1 \times 2$) supercell with the PW-LDA functional. Figures shown below display the autocorrelation functions (left panel) and the accumulation of the averaged HCACF (right panel) along x, y and z directions respectively. Each autocorrelation function corresponds to a trajectory. The oscillatory decay can be inspected in all autocorrelation functions but the accumulation along z direction dominates, which agrees with the assumption that the CH_2 chain lies along z direction.

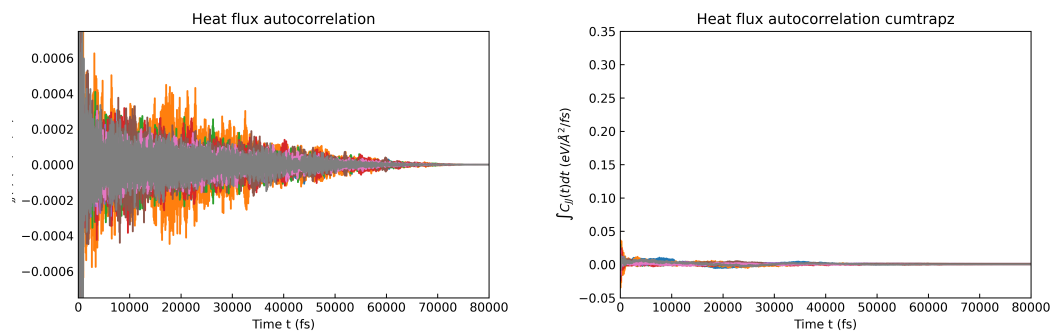


Figure 3.11.: The autocorrelation functions(left panel) and its integral(right panel) from multiple equilibrium molecular dynamics simulations along x direction.

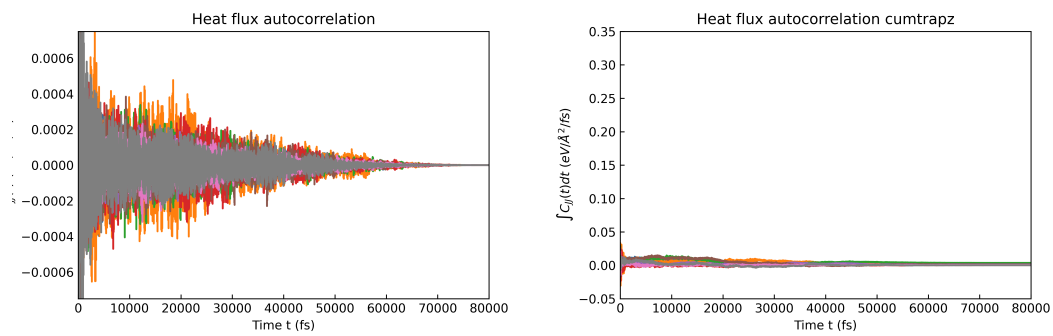


Figure 3.12.: The autocorrelation functions(left panel) and its integral(right panel) from multiple equilibrium molecular dynamics simulations along y direction.

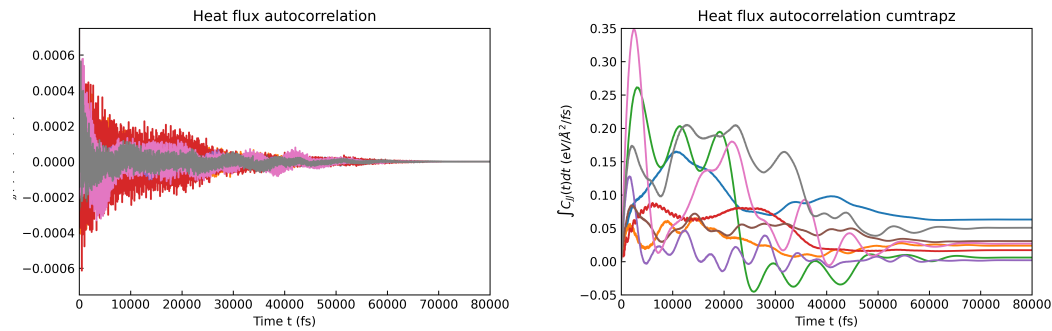


Figure 3.13.: The autocorrelation functions(left panel) and its integral(right panel) from multiple equilibrium molecular dynamics simulations along z direction.

3.4.2. Thermal conductivity by Green-Kubo method

The lattice thermal conductivity can be calculated by Green-Kubo formula through Eq. (2.5.38). For each starting conditions Γ_0^i chosen from the above NVT molecular dynamics simulations, NVE molecular dynamics simulations with *velocity Verlet algorithm* discussed in Sec. (2.4.1) are performed to generate the time evolution of the system Γ_t^i , and evaluate the heat flux, $J(t)$ along this trajectory. The final thermal conductivity with error bars is shown in Fig. (3.14). Clearly, the x and y components of kappa are nearly 0 which agrees with the fact that the vibration is limited to z direction. The thermal conductivity decreases with temperature even if it is already comparatively small value 0.1 W/mK . In addition, in order to inspect the simulation time convergence, every trajectory at 100K is truncated down to a length of 10 ps, and we applied the workflow presented before to each of the truncated trajectories. The final value of $0.27 \pm 0.25 \text{ W/mK}$ is approached within error bars after the 70000 time steps, which corresponds to a simulation time of 70ps.

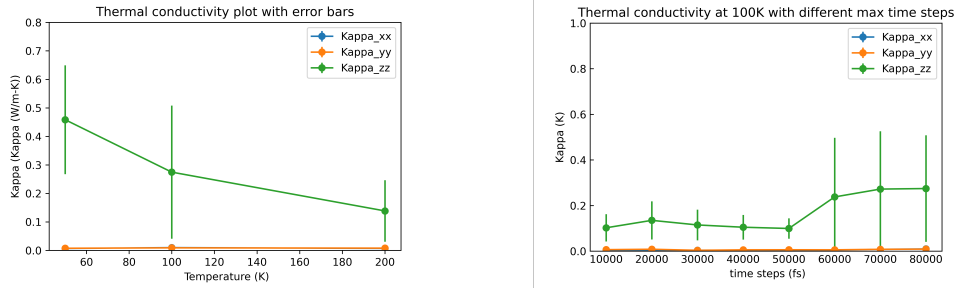


Figure 3.14.: Thermal conductivity at different Temperature(left panel) and the convergence in terms of the maximum time step(right panel).

The MD technique gives a deterministic non-quantum description of an N-atom system and temperature T_{MD} can be calculated from the mean kinetic energy E_c based on Boltzmann distribution function following the straightforward derivation

$$E_c = \frac{1}{2} M \sum_{i=1}^N v_i^2 = \frac{3}{2} N k_B T_{MD}. \quad (3.4.1)$$

The validity of relation shown in Eq. (3.4.1) holds only if the heat capacity is not temperature dependent i.e. temperature is greater than the Debye temperature, which however, does not apply to the results shown in Fig. (3.5). In this case, the true temperature gradient in the Fourier law must also be corrected according to

$$\frac{1}{\kappa_{MD}} \frac{dJ}{dT_{MD}} = \frac{1}{\kappa} \frac{dj}{dT} = \frac{1}{\kappa} \frac{dJ}{dT_{MD}} \frac{dT_{MD}}{dT}. \quad (3.4.2)$$

The quantum temperature T is obtained from

$$E = \int_0^{\infty} g(\omega) n(\omega, T) \hbar \omega d\omega \quad (3.4.3)$$

with phonon density of states $g(\omega)$ and Bose-Einstein distribution function $n(\omega, T)$. [63, 64] The thermal conductivity after quantum correction is therefore

$$\kappa = \kappa_{MD} \frac{dT_{MD}}{dT} = \kappa_{MD} \frac{c_v}{C_v^{MD}}. \quad (3.4.4)$$

To be more specific, the quantum specific heat at 200K can be read as $30 J/K/mol$ from Fig.(3.5) and the classic one is $3N_A k_B$ from *Dulong-Petit* law, $24.9 J/K/mol$. Thus, given the thermal conductivity from MD simulations at 200K, $0.13 W/mK$, the quantum-corrected thermal conductivity will be $0.11 W/mK$.

4. Properties of Magnesium oxide

Periclase magnesium oxide (MgO) is a well-known harmonic material which can be applied as a typical benchmark system for perturbative heat transport techniques. In this part, the vibrational properties of MgO are discussed and the thermal conductivity is calculated by means of lattice dynamics method and then compared with the literature. The primitive structure of MgO shown in Fig. (4.1) comes from *Material project* with the lattice constant $a=b=c=2.95\text{\AA}$. The red ball represents Oxygen atom and the yellow one is Magnesium atom. The unit cell for MgO has a rhombohedral crystal structure with the same lattice vector length and angles between each two of them are the same as well. Still, similar to what we have done in Sec. (3.1), the primitive structure is optimized with different Monkhorst-Pack grid and basis set. From the below Fig. (4.2), the total energy decreases with denser k grid and the relaxation by intermediate-default basis results in only 0.2 eV lower final energy than light default basis, which means the light basis set is good enough to satisfy the total energy convergence standard. In addition, both the energy and lattice constant qualitatively converge with k grid ($4 \times 4 \times 4$) with the Perdew-Wang LDA functional.

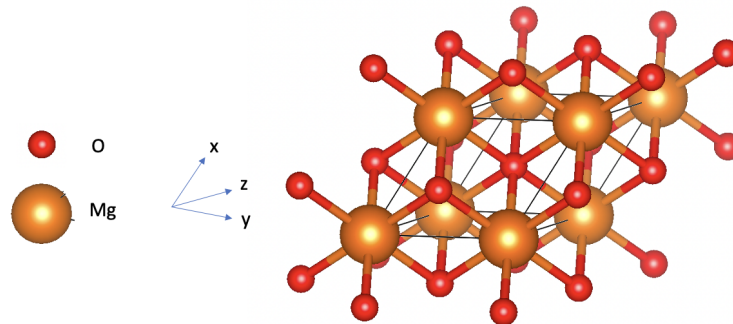


Figure 4.1.: Rhombohedral crystal structure of MgO with $a=b=c$ and $\alpha=\beta=\gamma$.

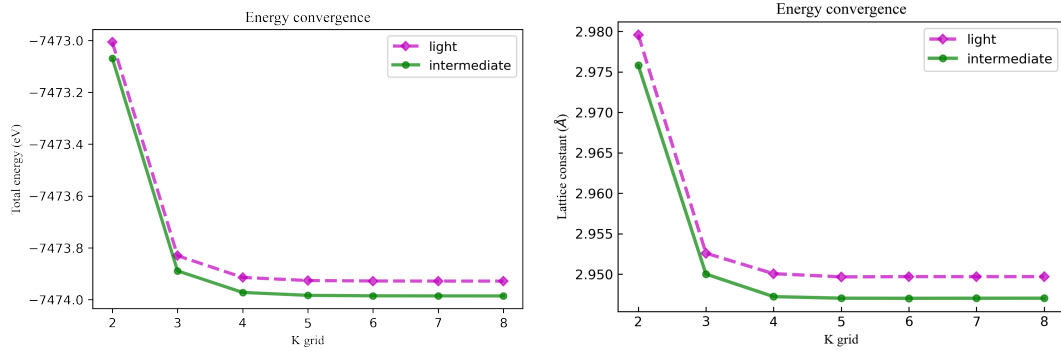


Figure 4.2.: Energy and lattice constant convergence with k grid and basis set for MgO crystal.

4.1. Vibrational Properties of MgO in the Harmonic Approximation

The phonon band structures for MgO are given by *phonopy-FHI-vibes* interface for conventional cubic $(1 \times 1 \times 1)$, $(2 \times 2 \times 2)$, $(3 \times 3 \times 3)$ and $(4 \times 4 \times 4)$ supercell containing 8, 64, 216, 512 atoms respectively, shown in Fig. (4.3). In comparison with the fully supercell converged $(3 \times 3 \times 3)$ band structure, the $(1 \times 1 \times 1)$ band structure exhibits e.g. over- and underestimated dispersion in the low or high frequency spectrum, and large deviations at the high-symmetry point L. Interestingly, the phonon branch does not split like the case in $(2 \times 2 \times 2)$, $(3 \times 3 \times 3)$ and $(4 \times 4 \times 4)$ supercells. This phonon mode splitting into two components can be associated with the symmetric and anti-symmetric displacements of the atoms[65]. On contrary, the $(2 \times 2 \times 2)$ band structure is essentially indistinguishable from the $(3 \times 3 \times 3)$ band structure at low frequencies (< 12 THz); for the high-frequency region, all qualitative features are well reproduced and only small quantitative deviations with a maximal value 2 THz are observed. Therefore, all calculations presented in next step were performed in a $(2 \times 2 \times 2)$ supercell with a good compromise between computational cost and accuracy.

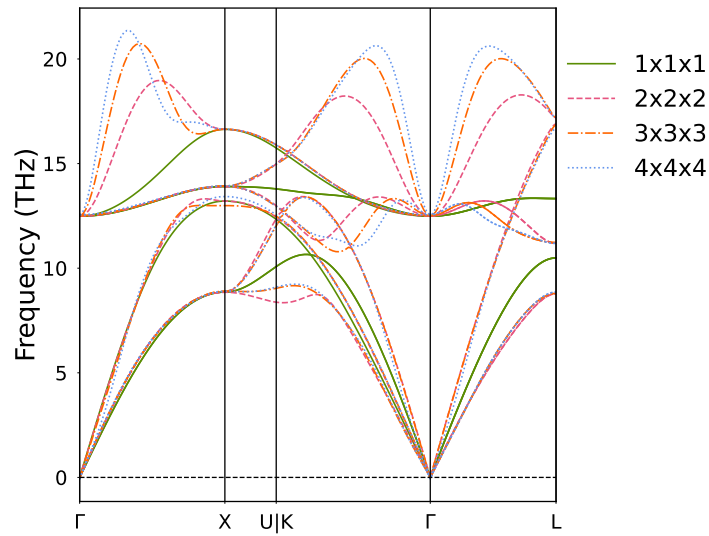


Figure 4.3.: Phonon band structure of MgO in the first (111), second (222), third (333) and fourth (444) cubic supercell calculated with PW-LDA functional and light basis set .

Additionally, Fig. (4.4) shows the thermodynamic potentials (free energy F and entropy S) and the respective specific heat C_v of MgO with respect to temperature, which were computed from the harmonic force constants with an extended $(45 \times 45 \times 45)$ \mathbf{q} grid as discussed in Sec. (2.3.1). It can be observed that the heat capacity is raised continuously on increasing in temperature and it has a typical quantum-mechanical T^3 dependence at low temperatures before approaching the classical Dulong-Petit limit at around 500K, which is consistent with the calculated and measured values.[66]

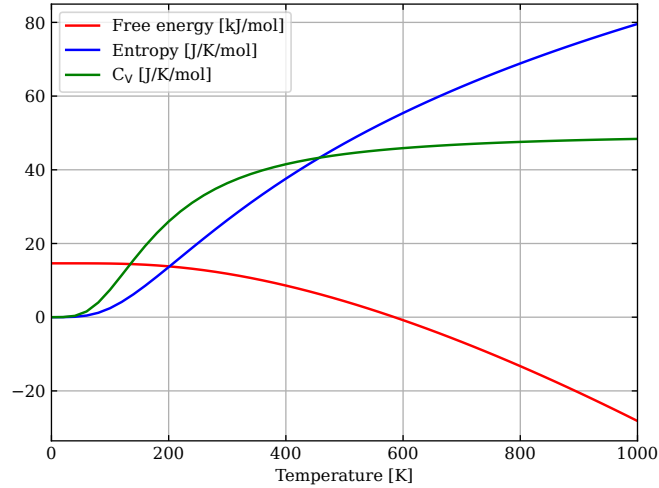


Figure 4.4.: Free energy and entropy of MgO and the respective specific heat C_v computed in the harmonic approximation. .

4.2. Lattice thermal conductivity by phono3py calculation

The vibrations of the atoms in a crystal can be described by a superposition of plane wave normal modes, ranging in frequency from the ultrasonic to the infrared regime. At high temperatures, the thermal equilibrium vibrational properties are dominated by the modes of highest frequency, but the lattice thermal conductivity depends on the behavior of waves at all frequencies. Exactly the same as the workflow in Sec. (3.2.1), the lattice thermal conductivity starts from computing the third order force constant followed by the lifetime and lastly kappa. Obviously, calculations on this structure requires more computational effort, generally in the order of $3N \times 3N \times 3N$, since it has a more complex structure, more atoms compared with the CH₂ chain in one dimension. However, similar to *phonopy* package, *phono3py* code package provides to reduce the computational effort by means of the symmetry. For example, only 194 structures were evaluated in a 64-atom ($2 \times 2 \times 2$) supercell. Even so, the computation load is much heavy for larger supercell. For 216-atom ($3 \times 3 \times 3$) and 512-atom ($4 \times 4 \times 4$) supercell, the third order constant(fc3) calculation requires 530 and 1122 structures. In this case, it is neither necessary nor possible to the compute some elements of supercell-fc3 if the interaction range of third order force

constant among triplets of atoms is expected to be shorter than chosen supercell size. This can be implemented in practice by the option *cutoff-pair-distance* provided in *phono3py*. The option *cutoff-pair-distance* has the same unit as the lattice constant, i.e. Å, whose upper limit is considered for convenience as the half of supercell size due to the minimum image convention while the lower limit will be the distance between two closest atoms. For instance, the cut-off distance is picked up from $(2 \times 2 \times 2)$ supercell as 2.5 Å, 3.0 Å, and 4.0 Å and so on, to inspect the influence of this parameter on the lattice thermal conductivity. For a periodic system, integrals in real space over the (infinitely extended) system are replaced by integrals over the (finite) first Brillouin zone in reciprocal space, by virtue of Bloch's theorem. In *FHI-aims*, such integrals are performed by summing the function values of the integrand, for instance, the charge density at a finite number of points in the Brillouin zone, called the q-point mesh. As the default behavior, the center of mesh is determined by the Monkhorst-Pack scheme as shown in 3.1. To be more specific, we take the cutoff 2.5 Å case as an example, where $(8 \times 8 \times 8)$ mesh, $(10 \times 10 \times 10)$ mesh, $(16 \times 16 \times 16)$ mesh and $(20 \times 20 \times 20)$ mesh are chosen to calculate the third order constant represented in Eq. (2.3.22) respectively, shown in Fig. (4.5).

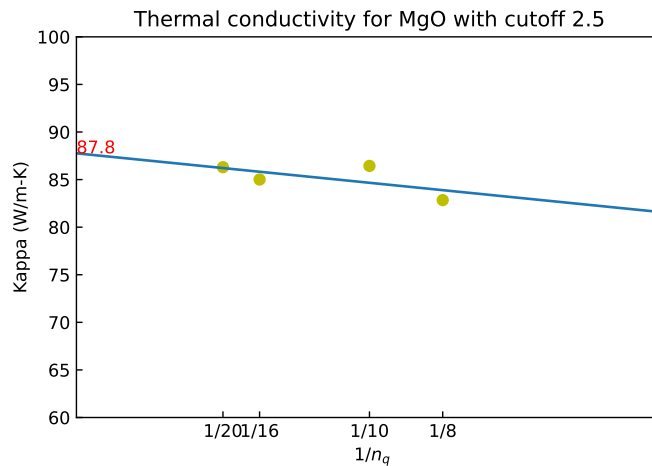


Figure 4.5.: Fitting and Extrapolation of the thermal conductivity for MgO $(2 \times 2 \times 2)$ supercell with cutoff pair distance 2.5 Å .

Then a linear fitting is applied and the fitting line is extrapolated to the infinity to represent the infinite integral. The intercept indicated in red color is the final thermal conductivity at

this cutoff distance. By repeating this process in other cutoff distances and other supercell, i.e. $(3 \times 3 \times 3)$, $(4 \times 4 \times 4)$ shown in Appendix A, the convergence in terms of the mesh size, cutoff distance and supercell size can be inspected. After the linear fitting and the results comparison between different cutoff distance, the thermal conductivity at 300K for $(2 \times 2 \times 2)$ and $(3 \times 3 \times 3)$ supercell are 89.8 ± 0.2 and 84.4 ± 0.8 W/mK . However, as we can see in Fig.(4.6), the thermal conductivity at 300K for MgO $(4 \times 4 \times 4)$ supercell is much smaller, with the value 69.2 ± 1.0 W/mK .

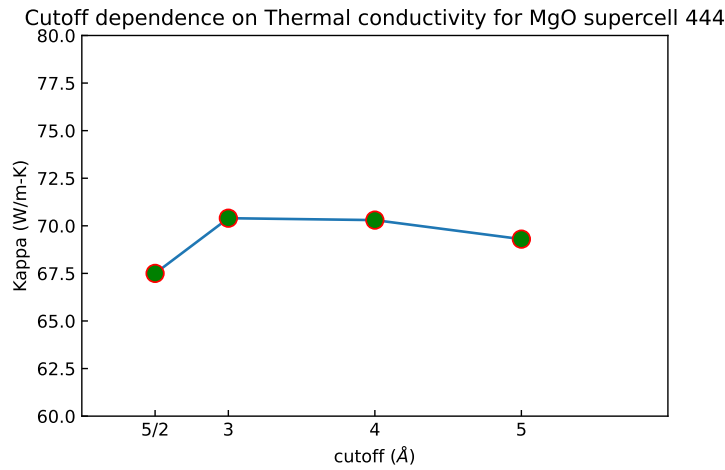


Figure 4.6.: Thermal conductivity with different cutoff distance after fitting and extrapolation for MgO $(4 \times 4 \times 4)$ supercell .

In order to validate our calculation results, experimental and theoretical studies on the lattice thermal conductivity under ambient pressure are shown in Fig. (4.7), where the dashed double-dotted line represents the *ab initio* anharmonic lattice dynamics simulations using the RTA with the isotopic correction[67]. It can be noticed that the value is around 65 W/mK , which is also similar to our calculation.

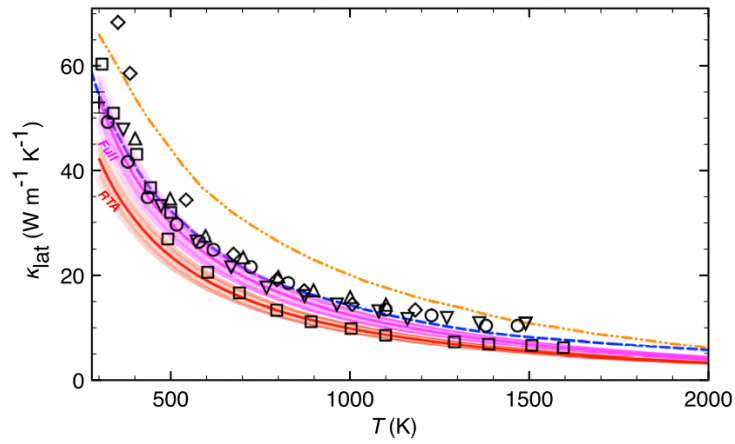


Figure 4.7.: Reference for thermal conductivity with temperature ranging from 300K to 1000K[68] .

Several more reference results from different groups are shown in Table (4.1). When compared with the literature, both experimental and theoretical values, the *phonopy* interface approaches a larger value which can be attributed to underestimated lattice constants due to the LDA functional[67] resulting in large discrepancies with measured values. Interestingly, if we compare the result from Green-Kubo calculation[54], $68.8 \pm 6.1 W/mK$ and lattice dynamics method, $69.2 \pm 1.0 W/mK$, it can be noticed that the results are quite close, which can be explained by the fact the MgO is a harmonic crystal and thus anharmonicity does not have much influence on the thermal conductivity.

Table 4.1.

	Reference	Thermal conductivity at 300K W/mK
Experiment	MacPherson and Schloessin[69]	61.7 ± 10.5
	Katsura[70]	65 ± 15
Theory	Hofmeister[71]	50.1
	de Koker[72] (LDA)	70.3 ± 8.9
	Dekura et.al[73] (LDA)	≈ 54
	Tang et al. [67] (LDA)	66
	Plata et al.[74] (PBE)	54.06
	Xia et al.[75] (PBE)	50.1-58.7
	Florian [54] (ai Green-Kubo)	68.8 ± 6.1

In addition, isotope effects have been reported that a simple isotope substitution has a surprisingly large impact on the lifetime of a specific mode and thus leads to a higher

thermal conductivity than the experimental results.[76] For instance, the thermal conductivity reaches its maximum at 227K for Si₁₉₂ and drops significantly with the isotope Si₁₈₂⁵⁶Si₁₀ which can be related to the localization of some impurity-related modes.[64] The average atomic masses directly affect the phonon frequencies via dynamic matrix and the three-phonon interaction strengths defined in Eq. (2.3.22). In *phono3py* packages, the natural mass variation at atomic sites can introduce additional isotope scattering and thus reduce the lattice thermal conductivity due to the presence of isotopes with different masses, which partly explains the overestimated values compared with the experiment results.

5. Thermal Conductivities for Strongly Anharmonic Compounds

In this section, we benchmark the lattice dynamics method on four model systems with high anharmonicity score to compare the accuracy of perturbative and non-perturbative GK calculations for realistic materials. We choose these materials from a set of compounds investigated with the GK method by Knoop[54]. The thermal conductivity for 33 materials without experimental reference by means of *ab initio* Green-Kubo methods is shown in Fig. (5.1), where the x axis indicates the anharmonicity discussed in Sec. (2.3.2), and their corresponding thermal conductivity can be read from the y axis. Figures and data for all compounds by *ab initio* Green-Kubo calculation are from Ref. [54].

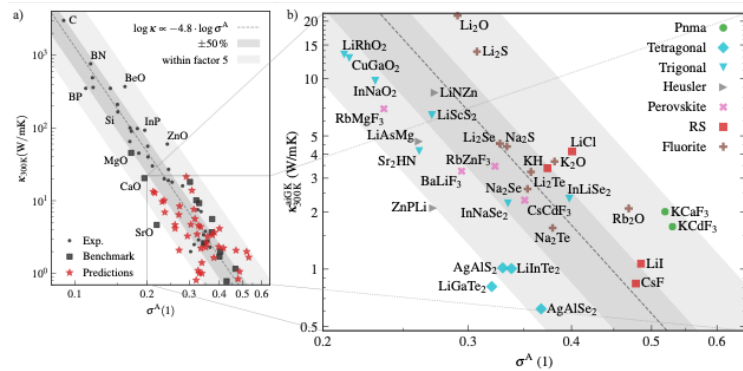


Figure 5.1.: Thermal conductivity at room temperature computed via *ab initio* Green Kubo (aiGK) vs. anharmonicity measure. Filled symbols denote materials without experimental reference. Fig. from Ref. [54].

The dashed diagonal line indicates an inverse linear fitting for the relationship between

the logarithms of thermal conductivity and anharmonicity for the binary materials in the dataset.

$$\kappa(\sigma^A) \approx 0.02 \cdot (\sigma^A)^{-4.8} \quad (5.0.1)$$

The light grey and the dark grey regions denote a deviation from the experiment with 50% and 15% respectively. This correlation implies an qualitative estimator for the thermal conductivity provided with the anharmonicity score without the requirement of further vibrational properties. Specifically, diamond, as an allotropy of carbon, possesses a well-known large thermal conductivity of 3000 W/mK [77] and therefore, the above linear fitting is intuitively correct since diamond is the most harmonic material. Stronger anharmonicity leads to shorter phonon lifetimes, which results in lower thermal conductivity according to Eq. (2.3.26). In the following step, LiGaTe_2 , CsF , LiI , KCaF_3 are used as a comparison to calculate their thermal conductivity at room temperature based on the lattice dynamics methods via *phono3py* package. All these materials show very low κ . While all these materials are far from harmonic, they differ in σ quite significantly. In addition, two geometries are considered, the one generated in 0K and the one considering lattice expansion at 300K. For each material, pair cutoff distance and the mesh size convergence on thermal conductivity are inspected and presented along with other supplementary in the Appendix B for simplicity. The convergence procedure is the same as the process discussed for the MgO calculation.

Rock salt structures CsF and LiI

Firstly, we take a look at the simple binary material CsF and LiI , which both have rock salt crystal structure, as shown in Fig. (5.2). The supercell size is constructed as conventional cubic ($3 \times 3 \times 3$), containing 216 atoms, which gives the phonon band structures shown in Fig. (5.3).

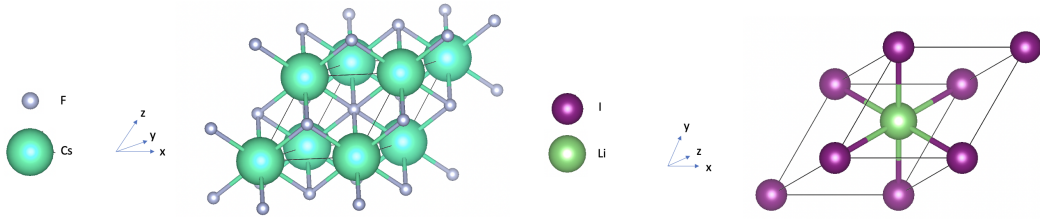


Figure 5.2.: Crystal structure of binary cubic rock salt CsF and LiI .

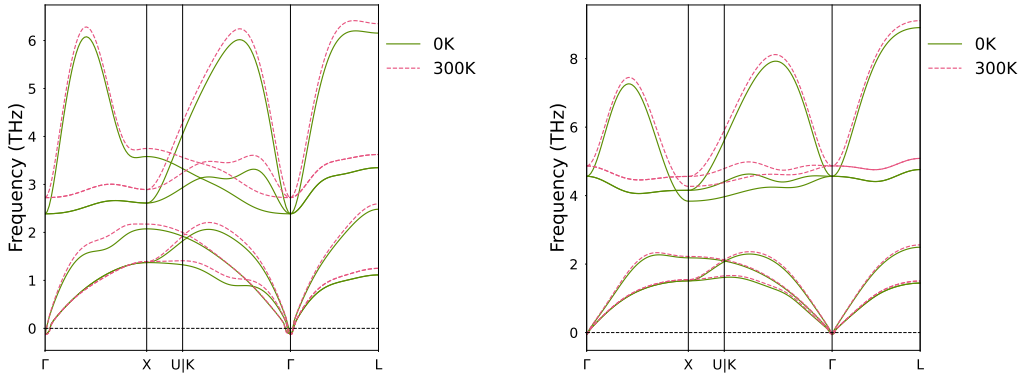


Figure 5.3.: Phonon band structure for CsF(left panel) and LiI(right panel) with or without lattice expansion

It can be noticed that for each material accounting for lattice expansion only increases the frequency slightly and the shape of the optical branches are similar except that the maximum frequency for CsF is 6 THz while around 8 THz for LiI, which implies that the thermal conductivity for LiI should be a bit larger than that for CsF. This hint is then proved by the following *phono3py* calculation, shown in Fig. (5.4) and Fig. (5.5), where among the total 530 structures, more than 300 structures are calculated with the cutoff distance 10 \AA . The thermal conductivity for CsF at room temperature is $0.83 \pm 0.05 \text{ W/mK}$ without considering the lattice expansion but it will be $1.2 \pm 0.1 \text{ W/mK}$ if the lattice is expanded. This discrepancy due to the thermal expansion is not observed in LiI, where in both condition, a kappa value of $1.4 \pm 0.1 \text{ W/mK}$ is obtained. The thermal conductivity obtained via the aiGK method including lattice expansion is lower by 0.36 and 0.33 W/mK , and they are 0.84 and 1.07 W/mK for CsF and LiI respectively, which corresponds to a relative error of 42.8% and 30.8%.

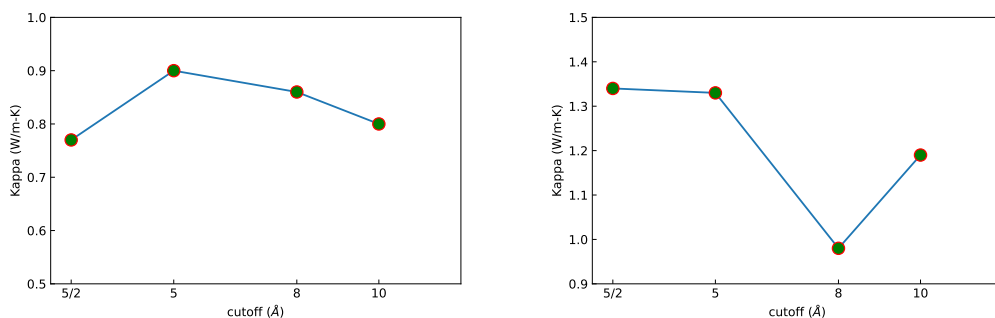


Figure 5.4.: Cutoff distance convergence on thermal conductivity at 300K for CsF with(left panel) or without(right panel) lattice expansion.

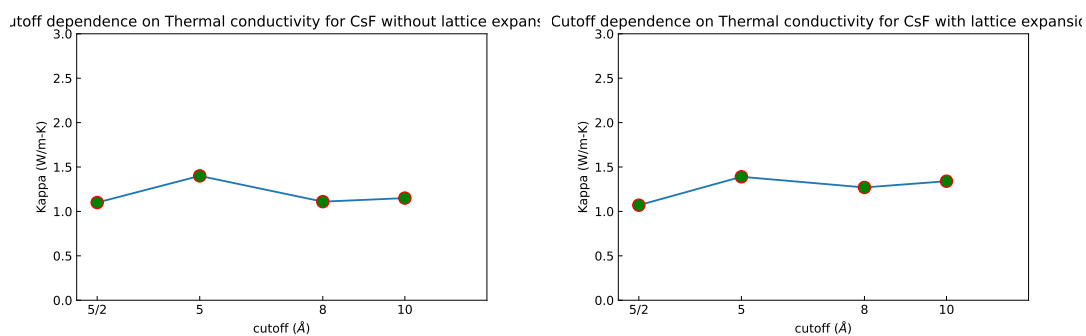


Figure 5.5.: Cutoff distance convergence on thermal conductivity at 300K for LiI with(left panel) or without(right panel) lattice expansion.

Perovskites KCaF_3

For the strongly anharmonic perovskites compounds KCaF_3 , ($3 \times 3 \times 3$) conventional standard supercell containing 158 atoms is calculated for 14931 displacement, among which 2613 structures are considered by setting the cutoff distance as 5 Å. The phonon band structure shown in the right panel of Fig. (5.6) suggests a larger kappa than CsF and LiI since the maximum frequency of approximately 13 THz is higher. However, this is not the case in the lattice dynamics calculation shown in Fig. (5.7).

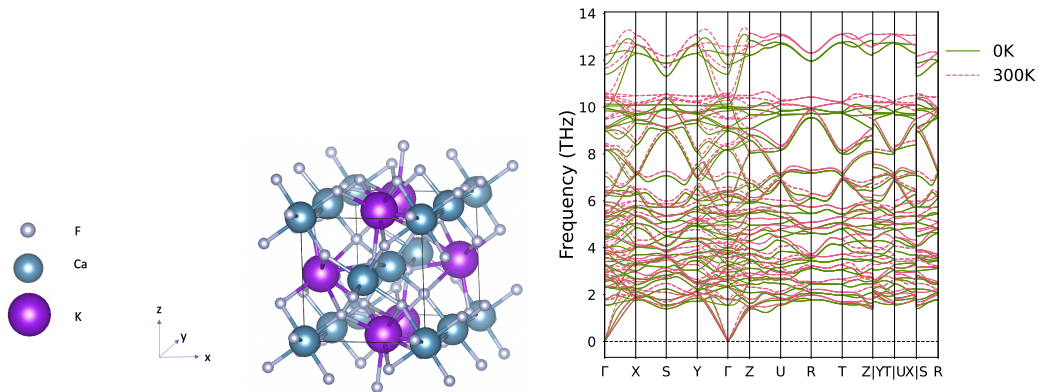


Figure 5.6.: Crystal structure and phonon band structure for KCaF_3 .

It can be observed that with more calculated structures by adjusting the pair cutoff distance, the thermal conductivity decreases for both situation considering the lattice expansion or not. The convergence appears at 5 \AA with the thermal conductivity at 300K 0.7 and 1.0 W/mK without or with thermal expansion respectively. Compared in the *aiGK* calculations, κ is under-estimated considerably by 100%, for KCaF_3 with 1.0 W/mK compared to 2 W/mK in GK calculation. This is a result of the large anharmonicity force contributions, which makes up nearly 60% of the total force as discussed in Sec. (2.4.4). Its large anharmonicity means that the cubic and higher-order anharmonic terms in Born–Oppenheimer (BO) energy surface can not be considered as small perturbations. Interestingly, these higher order terms appear to increase the thermal conductivity. This is consistent with the fact that KCaF_3 is known to undergo a phase transition to a higher-symmetry structure, which is not accounted for in perturbative approaches.

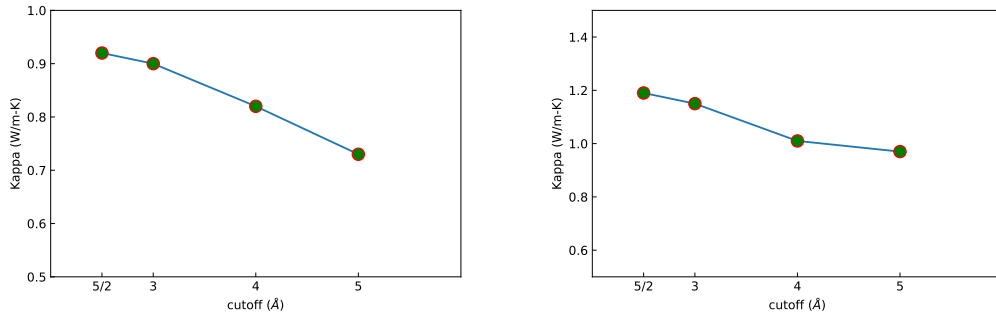


Figure 5.7.: Cutoff distance convergence on thermal conductivity at 300K for KCaF with(left panel) or without(right panel) lattice expansion.

Ternary chalcopyrite LiGaTe₂

Li-containing ternary chalcopyrite compounds have been reported to possess nonzero second order nonlinear susceptibility.[78] Thermal conductivity is important for the optical properties in the efficiency of the outputs of the devices by affecting the absorption of optical energy.[79] In order to calculate the phonon band structure, the supercell matrix

is chosen as $\begin{pmatrix} 0 & 3 & 3 \\ 3 & 0 & 3 \\ 1 & 1 & -1 \end{pmatrix}$, so the supercell contains 216 atoms. It can be observed that

in the right panel of Fig. (5.8), the optical branches are flat and non-dispersive, which correspond to localized atomic motion in the system and therefore carry little heat.

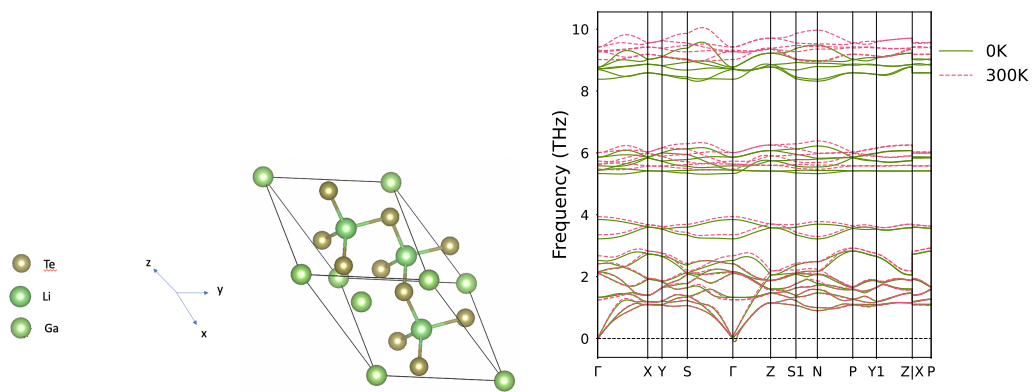


Figure 5.8.: Crystal structure and phonon band structure for LiGaTe_2 .

Due to the large amount of the 31128 total structures, a small cutoff distance 4 \AA is chosen to save the computational effort. In this case, 744 structures are calculated and the resulted thermal conductivity is 1.25 W/mK at 300K. This value is a bit larger than the aiGK calculation result $0.81 \pm 0.15 \text{ W/mK}$ with a relative error of 54.3%, which can be attributed to the strong scattering of phonon quasiparticles by anharmonicity[80].

6. Conclusion

Thermal conductivity characterizes the ability of the material to transfer the heat, which is essential in thermoelectric devices design. In this work, in order to calculate the thermal conductivity, lattice dynamics method based on phonon scatterings and *ab initio* Greenkubo method are employed and compared. The calculation on CH₂ chain shows a simple example of the work flow of aiGK method and the following MgO calculation explains the lattice dynamic method realized by *phono3py* package. In the last part, the benchmark based on 4 strong anharmonic materials shows that anharmonicity score gives a hint to choose the suitable method. Generally, when the anharmonicity is small, both lattice dynamic method and *aiGK* method provide acceptable results, for example MgO. On the contrary, if the material exhibits strong anharmonicity, aiGK method can differ from LD methods quite significantly. Although absolute errors are relatively small ($< 1 \text{ W/mK}$), relative errors can be as large as 100%. As a consequence, both methods predict the materials to be insulating, but the actual ranking differs, since higher-order terms can both increase and decrease the thermal conductivity. For accurate predictions in the W/mK-regime, the *aiGK* method should thus be used to account for the anharmonicity. Nevertheless, more materials should be further calculated to give a more general criterion.

Bibliography

- [1] Volker Haigis, Mathieu Salanne, and Sandro Jahn. “Thermal conductivity of MgO, MgSiO₃ perovskite and post-perovskite in the Earth’s deep mantle”. In: *Earth and Planetary Science Letters* 355 (2012), pp. 102–108.
- [2] Umish Srivastva, RK Malhotra, and SC Kaushik. “Review of heat transport properties of solar heat transfer fluids”. In: *Journal of Thermal Analysis and Calorimetry* 130.2 (2017), pp. 605–621.
- [3] Hans Janssen, Bert Blocken, and Jan Carmeliet. “Conservative modelling of the moisture and heat transfer in building components under atmospheric excitation”. In: *International Journal of Heat and Mass Transfer* 50.5-6 (2007), pp. 1128–1140.
- [4] Matthew C Wingert et al. “Thermal transport in amorphous materials: a review”. In: *Semiconductor Science and Technology* 31.11 (2016), p. 113003.
- [5] Gangjian Tan, Li-Dong Zhao, and Mercouri G Kanatzidis. “Rationally designing high-performance bulk thermoelectric materials”. In: *Chemical reviews* 116.19 (2016), pp. 12123–12149.
- [6] Ssenoga Twaha et al. “A comprehensive review of thermoelectric technology: Materials, applications, modelling and performance improvement”. In: *Renewable and sustainable energy reviews* 65 (2016), pp. 698–726.
- [7] Hilaal Alam and Seeram Ramakrishna. “A review on the enhancement of figure of merit from bulk to nano-thermoelectric materials”. In: *Nano energy* 2.2 (2013), pp. 190–212.
- [8] Paothep Pichanusakorn and Prabhakar Bandaru. “Nanostructured thermoelectrics”. In: *Materials Science and Engineering: R: Reports* 67.2-4 (2010), pp. 19–63.
- [9] H Julian Goldsmid et al. *Introduction to thermoelectricity*. Vol. 121. Springer, 2010.
- [10] A Zolriasatein et al. “Influence of PCA on thermoelectric properties and hardness of nanostructured Ba–Cu–Si clathrates”. In: *Materials & Design* 87 (2015), pp. 883–890.

-
-
- [11] Gayatri Keskar et al. “Significant improvement of thermoelectric performance in nanostructured bismuth networks”. In: *Nano Energy* 1.5 (2012), pp. 706–713.
- [12] Ripeng Luo and Kuang Yu. “Capturing the nuclear quantum effects in molecular dynamics for lattice thermal conductivity calculations: Using ice as example”. In: *The Journal of Chemical Physics* 153.19 (2020), p. 194105.
- [13] DA Broido, A Ward, and N Mingo. “Lattice thermal conductivity of silicon from empirical interatomic potentials”. In: *Physical Review B* 72.1 (2005), p. 014308.
- [14] Atsushi Togo and Isao Tanaka. “First principles phonon calculations in materials science”. In: *Scripta Materialia* 108 (2015), pp. 1–5.
- [15] Patrick K Schelling, Simon R Phillpot, and Pawel Keblinski. “Comparison of atomic-level simulation methods for computing thermal conductivity”. In: *Physical Review B* 65.14 (2002), p. 144306.
- [16] Stefano Baroni et al. “Heat transport in insulators from ab initio Green-Kubo theory”. In: *Handbook of materials modeling: Applications: Current and emerging materials* (2020), pp. 809–844.
- [17] Arian Berger et al. “Impact of nuclear quantum effects on the structural inhomogeneity of liquid water”. In: *Proceedings of the National Academy of Sciences* 116.7 (2019), pp. 2458–2463.
- [18] Nina Shulumba, Olle Hellman, and Austin J Minnich. “Lattice thermal conductivity of polyethylene molecular crystals from first-principles including nuclear quantum effects”. In: *Physical review letters* 119.18 (2017), p. 185901.
- [19] Franz Knuth et al. “All-electron formalism for total energy strain derivatives and stress tensor components for numeric atom-centered orbitals”. In: *Computer Physics Communications* 190 (2015), pp. 33–50.
- [20] Volker Blum et al. “Ab initio molecular simulations with numeric atom-centered orbitals”. In: *Computer Physics Communications* 180.11 (2009), pp. 2175–2196.
- [21] Florian Knoop et al. “FHI-vibes: Ab Initio Vibrational Simulations”. In: *The Journal of Open Source Software* 5.56 (2020).
- [22] Ask Hjorth Larsen et al. “The atomic simulation environment—a Python library for working with atoms”. In: *Journal of Physics: Condensed Matter* 29.27 (2017), p. 273002.
- [23] Robert G Parr and Yang Weitao. “Chemical potential derivatives”. In: *Density-Functional Theory of Atoms and Molecules*. Oxford University Press, 1989.

-
-
- [24] P Hohenberg and WJPR Kohn. “Density functional theory (DFT)”. In: *Phys. Rev* 136 (1964), B864.
- [25] Biswajit Santra. “Density-functional theory exchange-correlation functionals for hydrogen bonds in water”. PhD thesis. Technische Universität Berlin Berlin, 2010.
- [26] John P Perdew and Karla Schmidt. “Jacob’s ladder of density functional approximations for the exchange-correlation energy”. In: *AIP Conference Proceedings*. Vol. 577. American Institute of Physics. 2001, pp. 1–20.
- [27] E Fermi and F Zeit. “Physik 48, 73 (1928); LH Thomas”. In: *Proc. Camb. Phil. Soc.* Vol. 23. 1927, p. 542.
- [28] John P Perdew, Kieron Burke, and Matthias Ernzerhof. “Generalized gradient approximation made simple”. In: *Physical review letters* 77.18 (1996), p. 3865.
- [29] John P Perdew et al. “Restoring the density-gradient expansion for exchange in solids and surfaces”. In: *Physical review letters* 100.13 (2008), p. 136406.
- [30] John P Perdew, P Ziesche, and H Eschrig. *Electronic structure of solids’ 91*. 1991.
- [31] Jochen Heyd, Gustavo E Scuseria, and Matthias Ernzerhof. “Hybrid functionals based on a screened Coulomb potential”. In: *The Journal of chemical physics* 118.18 (2003), pp. 8207–8215.
- [32] Neil W Ashcroft, N David Mermin, et al. *Solid state physics*. 1976.
- [33] Slawomir Biernacki and Matthias Scheffler. “Negative thermal expansion of diamond and zinc-blende semiconductors”. In: *Physical review letters* 63.3 (1989), p. 290.
- [34] Karena W Chapman and Peter J Chupas. “Pressure enhancement of negative thermal expansion behavior and induced framework softening in zinc cyanide”. In: *Journal of the American Chemical Society* 129.33 (2007), pp. 10090–10091.
- [35] Pinku Nath et al. “High-throughput prediction of finite-temperature properties using the quasi-harmonic approximation”. In: *Computational Materials Science* 125 (2016), pp. 82–91.
- [36] RA Cowley. “Anharmonicity”. In: *J. Phys.(Paris)* 26.3 (1965), pp. 659–664.
- [37] A Debernardi et al. “Anharmonic self-energy of phonons: Ab initio calculations and neutron spin echo measurements”. In: *arXiv preprint cond-mat/0212209* (2002).
- [38] José Menéndez and Manuel Cardona. “Temperature dependence of the first-order Raman scattering by phonons in Si, Ge, and α -Sn: Anharmonic effects”. In: *Physical Review B* 29.4 (1984), p. 2051.

-
- [39] Laurent Chaput. “Direct solution to the linearized phonon Boltzmann equation”. In: *Physical review letters* 110.26 (2013), p. 265506.
- [40] Atsushi Togo, Laurent Chaput, and Isao Tanaka. “Distributions of phonon lifetimes in Brillouin zones”. In: *Physical Review B* 91.9 (2015), p. 094306.
- [41] Alan JH McGaughey and M Kaviani. “Quantitative validation of the Boltzmann transport equation phonon thermal conductivity model under the single-mode relaxation time approximation”. In: *Physical Review B* 69.9 (2004), p. 094303.
- [42] Si-ping Han et al. “Thermal decomposition of condensed-phase nitromethane from molecular dynamics from ReaxFF reactive dynamics”. In: *The Journal of Physical Chemistry B* 115.20 (2011), pp. 6534–6540.
- [43] Yifei Mo, Shyue Ping Ong, and Gerbrand Ceder. “First principles study of the Li₁₀GeP₂S₁₂ lithium super ionic conductor material”. In: *Chemistry of Materials* 24.1 (2012), pp. 15–17.
- [44] Yifei Mo, Shyue Ping Ong, and Gerbrand Ceder. “Insights into diffusion mechanisms in P2 layered oxide materials by first-principles calculations”. In: *Chemistry of Materials* 26.18 (2014), pp. 5208–5214.
- [45] Xingfeng He and Yifei Mo. “Accelerated materials design of Na_{0.5}Bi_{0.5}TiO₃ oxygen ionic conductors based on first principles calculations”. In: *Physical Chemistry Chemical Physics* 17.27 (2015), pp. 18035–18044.
- [46] Xingfeng He, Yizhou Zhu, and Yifei Mo. “Origin of fast ion diffusion in super-ionic conductors”. In: *Nature communications* 8.1 (2017), pp. 1–7.
- [47] Zhi Deng, Yifei Mo, and Shyue Ping Ong. “Computational studies of solid-state alkali conduction in rechargeable alkali-ion batteries”. In: *NPG Asia Materials* 8.3 (2016), e254–e254.
- [48] TH Lee and SR Elliott. “Ab initio computer simulation of the early stages of crystallization: Application to Ge₂Sb₂Te₅ phase-change materials”. In: *Physical Review Letters* 107.14 (2011), p. 145702.
- [49] Xingfeng He et al. “Statistical variances of diffusional properties from ab initio molecular dynamics simulations”. In: *npj Computational Materials* 4.1 (2018), pp. 1–9.
- [50] Jos Thijssen. *Computational physics*. Cambridge university press, 2007.
- [51] D West and SK Estreicher. “First-principles calculations of vibrational lifetimes and decay channels: Hydrogen-related modes in Si”. In: *Physical review letters* 96.11 (2006), p. 115504.

-
-
- [52] Bin Wei et al. “Phonon anharmonicity: a pertinent review of recent progress and perspective”. In: *Science China Physics, Mechanics & Astronomy* 64.11 (2021), pp. 1–34.
- [53] Florian Knoop et al. “Anharmonicity measure for materials”. In: *Physical Review Materials* 4.8 (2020), p. 083809.
- [54] Florian Knoop. “Heat transport in strongly anharmonic solids from first principles”. In: (2022).
- [55] Bingqing Cheng and Daan Frenkel. “Computing the heat conductivity of fluids from density fluctuations”. In: *Physical Review Letters* 125.13 (2020), p. 130602.
- [56] Laura de Sousa Oliveira and P Alex Greaney. “Thermal resistance from irradiation defects in graphite”. In: *Computational Materials Science* 103 (2015), pp. 68–76.
- [57] Christian Carbogno, Rampi Ramprasad, and Matthias Scheffler. “Ab initio Green-Kubo approach for the thermal conductivity of solids”. In: *Physical review letters* 118.17 (2017), p. 175901.
- [58] Alper Kinaci, Justin B Haskins, and Tahir Çağın. “On calculation of thermal conductivity from Einstein relation in equilibrium molecular dynamics”. In: *The Journal of chemical physics* 137.1 (2012), p. 014106.
- [59] R Vogelsang, C Hoheisel, and G Ciccotti. “Thermal conductivity of the Lennard-Jones liquid by molecular dynamics calculations”. In: *The Journal of chemical physics* 86.11 (1987), pp. 6371–6375.
- [60] GD Harp and BJ Berne. “Time-correlation functions, memory functions, and molecular dynamics”. In: *Physical Review A* 2.3 (1970), p. 975.
- [61] Hendrik J Monkhorst and James D Pack. “Special points for Brillouin-zone integrations”. In: *Physical review B* 13.12 (1976), p. 5188.
- [62] Tue Gunst et al. “First-principles method for electron-phonon coupling and electron mobility: Applications to two-dimensional materials”. In: *Physical Review B* 93.3 (2016), p. 035414.
- [63] S Volz et al. “Computation of thermal conductivity of Si/Ge superlattices by molecular dynamics techniques”. In: *Microelectronics Journal* 31.9-10 (2000), pp. 815–819.
- [64] TM Gibbons, SK Estreicher, Christian Carbogno, et al. “Thermal conductivity of Si nanostructures containing defects: Methodology, isotope effects, and phonon trapping”. In: *Physical Review B* 84.3 (2011), p. 035317.

-
- [65] Sanjeev K Gupta, Himadri R Soni, and Prafulla K Jha. “Electronic and phonon bandstructures of pristine few layer and metal doped graphene using first principles calculations”. In: *AIP Advances* 3.3 (2013), p. 032117.
- [66] UC Srivastava and SP Singh. “Thermophysical and Ultrasonic Properties on Magnesium Oxide”. In: *International Journal of Recent Technology and Engineering (IJRTE)* (2019).
- [67] Xiaoli Tang and Jianjun Dong. “Lattice thermal conductivity of MgO at conditions of Earth’s interior”. In: *Proceedings of the National Academy of Sciences* 107.10 (2010), pp. 4539–4543.
- [68] Haruhiko Dekura, Taku Tsuchiya, et al. “Ab initio lattice thermal conductivity of MgO from a complete solution of the linearized Boltzmann transport equation”. In: *Physical Review B* 95.18 (2017), p. 184303.
- [69] WR MacPherson and HH Schloessin. “Apparent, lattice and radiative, thermal conductivity at temperatures from 300 to 1500 K and pressures up to 5.6 GPa: results for MgO and NaCl”. In: *High Temperatures. High Pressures* 15.5 (1983), pp. 495–509.
- [70] Tomoo Katsura. “Thermal diffusivity of periclase at high temperatures and high pressures”. In: *Physics of the earth and planetary interiors* 101.1-2 (1997), pp. 73–77.
- [71] Anne M Hofmeister. “Thermal diffusivity and thermal conductivity of single-crystal MgO and Al₂O₃ and related compounds as a function of temperature”. In: *Physics and Chemistry of Minerals* 41.5 (2014), pp. 361–371.
- [72] Nico de Koker. “Thermal conductivity of MgO periclase at high pressure: Implications for the D ”region”. In: *Earth and Planetary Science Letters* 292.3-4 (2010), pp. 392–398.
- [73] S Andersson and G Bäckström. “Techniques for determining thermal conductivity and heat capacity under hydrostatic pressure”. In: *Review of scientific instruments* 57.8 (1986), pp. 1633–1639.
- [74] Jose J Plata et al. “An efficient and accurate framework for calculating lattice thermal conductivity of solids: AFLOW—AAPL Automatic Anharmonic Phonon Library”. In: *npj Computational Materials* 3.1 (2017), pp. 1–10.
- [75] Yi Xia et al. “High-throughput study of lattice thermal conductivity in binary rocksalt and zinc blende compounds including higher-order anharmonicity”. In: *Physical Review X* 10.4 (2020), p. 041029.

-
- [76] KK Kohli et al. “Isotope Dependence of the Lifetime of the 1136- cm- 1 Vibration of Oxygen in Silicon”. In: *Physical review letters* 96.22 (2006), p. 225503.
- [77] Alistair Ward et al. “Ab initio theory of the lattice thermal conductivity in diamond”. In: *Physical Review B* 80.12 (2009), p. 125203.
- [78] L Isaenko et al. “Growth and properties of LiGaX₂ (X= S, Se, Te) single crystals for nonlinear optical applications in the mid-IR”. In: *Crystal Research and Technology: Journal of Experimental and Industrial Crystallography* 38.3-5 (2003), pp. 379–387.
- [79] J Donald Beasley. “Thermal conductivities of some novel nonlinear optical materials”. In: *Applied optics* 33.6 (1994), pp. 1000–1003.
- [80] Jingxuan Ding et al. “Anharmonic lattice dynamics and superionic transition in AgCrSe₂”. In: *Proceedings of the National Academy of Sciences* 117.8 (2020), pp. 3930–3937.



Acknowledgements

I appreciate the opportunity to do master thesis in NOMAD Laboratory of Fritz Haber Institute, Berlin. I would also like to acknowledge Dr. Christian Carbogno as the second reader of this thesis, and I am gratefully indebted to his very valuable comments on this thesis. Last but not least, I recognize the guidance from Henrik and Florian from NOMAD. This thesis will not be possible without their help.

A. Thermal conductivity for MgO with different supercell size

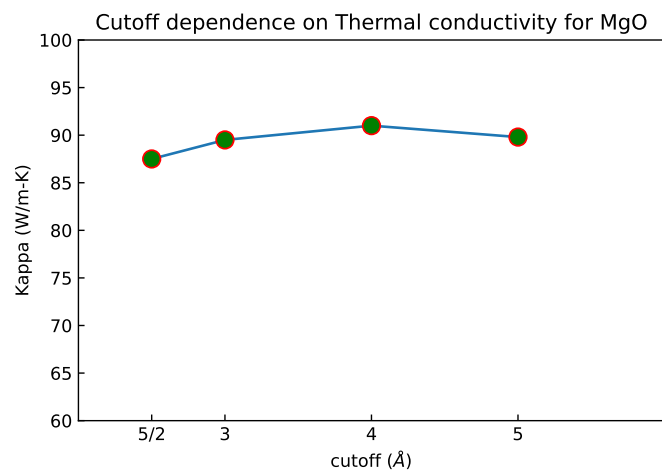


Figure A.2.: Thermal conductivity with different cutoff distance after fitting and extrapolation for MgO ($2 \times 2 \times 2$) supercell .

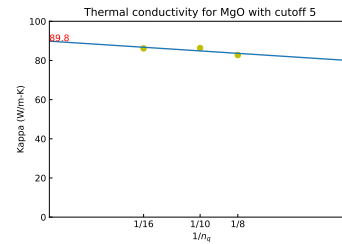
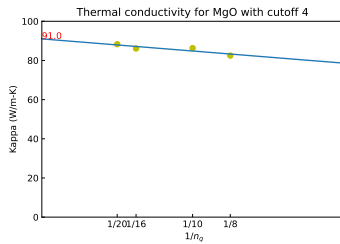
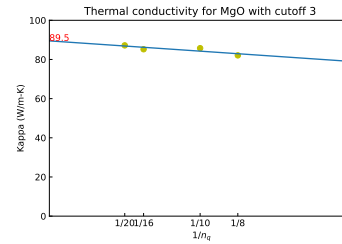
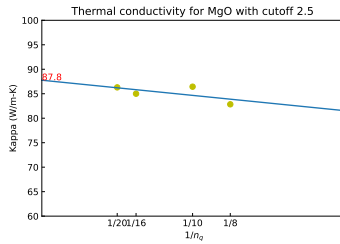


Figure A.1.: Fitting and extrapolation of thermal conductivity for supercell ($2 \times 2 \times 2$) at 300K with different cutoff distance.

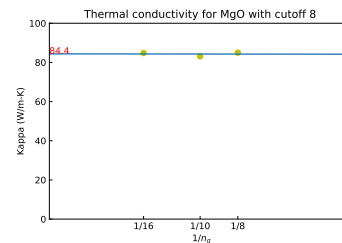
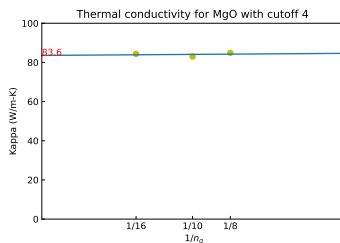
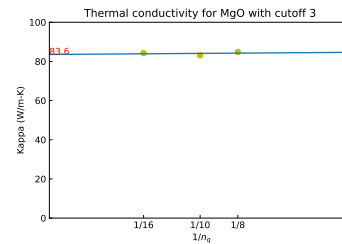
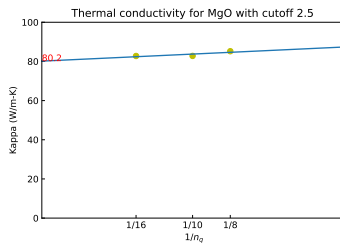


Figure A.3.: Fitting and extrapolation of thermal conductivity for supercell ($2 \times 2 \times 2$) at 300K with different cutoff distance.

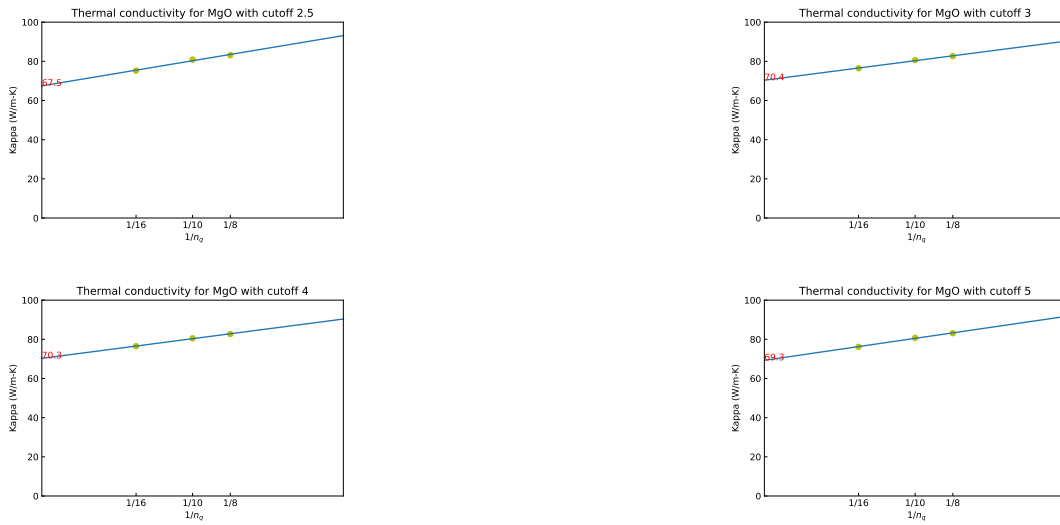


Figure A.5.: Fitting and extrapolation of thermal conductivity for supercell ($4 \times 4 \times 4$) at 300K with different cutoff distance.

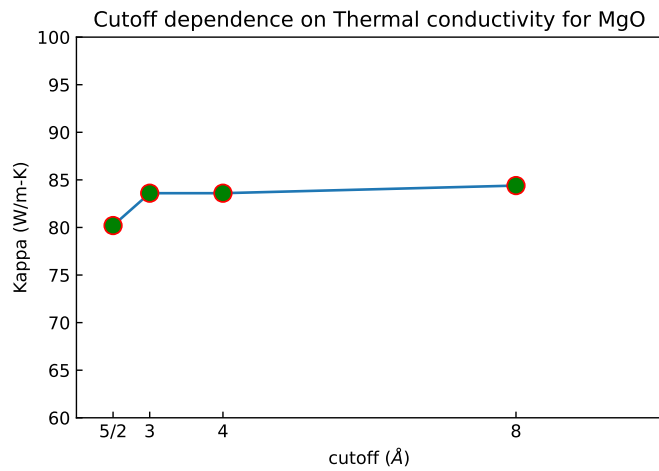


Figure A.4.: Thermal conductivity with different cutoff distance after fitting and extrapolation for MgO ($3 \times 3 \times 3$) supercell .

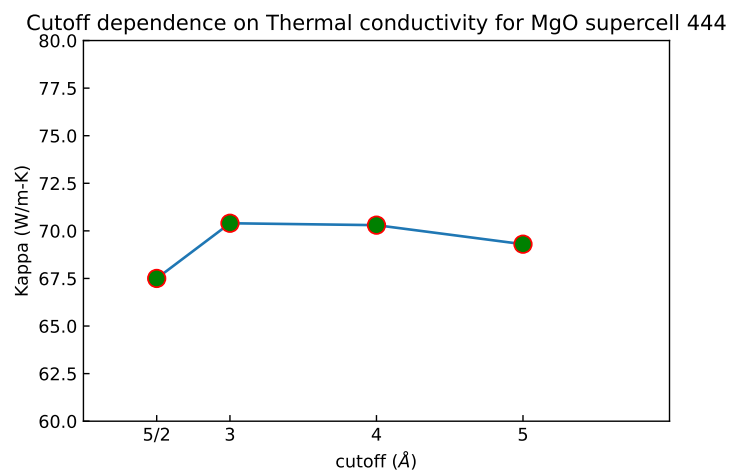


Figure A.6.: Thermal conductivity with different cutoff distance after fitting and extrapolation for MgO ($4 \times 4 \times 4$) supercell .

B. Vibrational properties of Strongly Anharmonic CsF

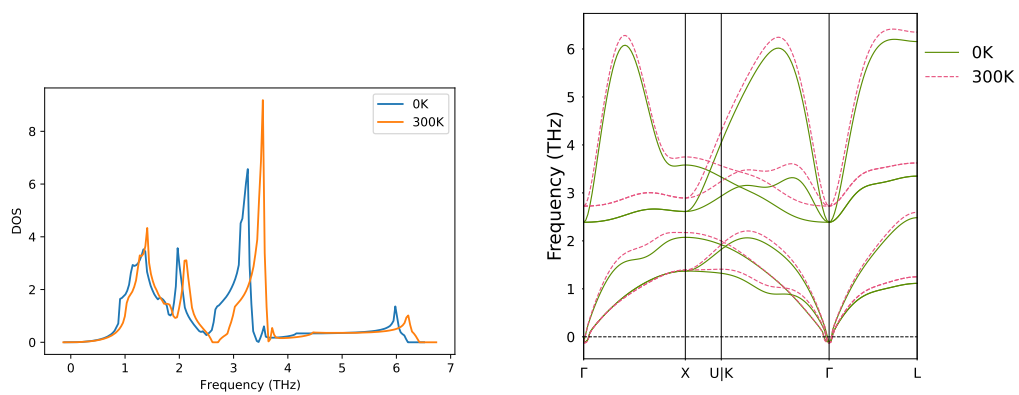
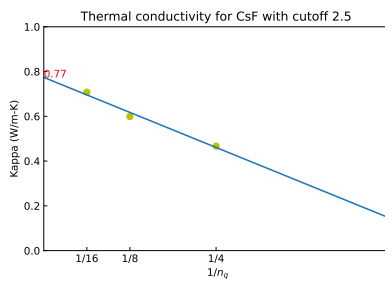
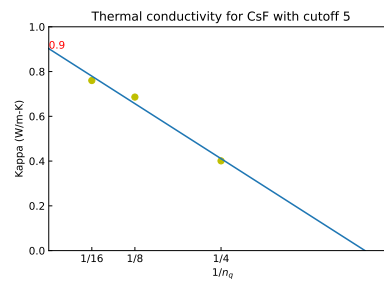


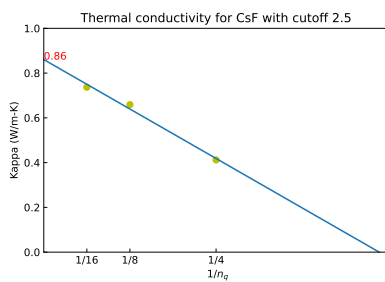
Figure B.1.: Phonon band structure and DOS for CsF



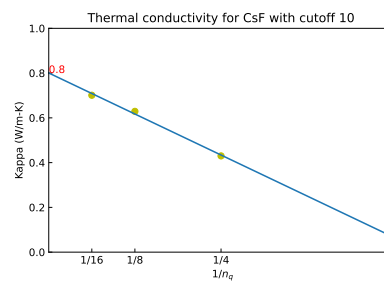
(a) Thermal conductivity for CsF with cutoff distance 2.5 Å.



(b) Thermal conductivity for CsF with cutoff distance 5 Å.

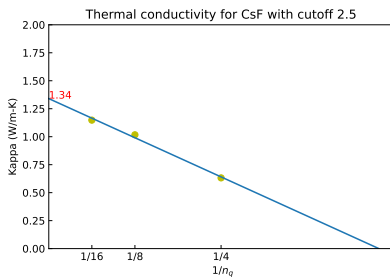


(c) Thermal conductivity for CsF with cutoff distance 8 Å.

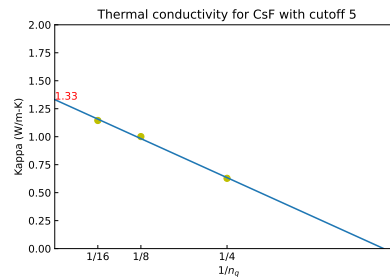


(d) Thermal conductivity for CsF with cutoff distance 10 Å.

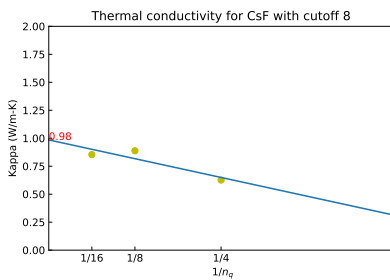
Figure B.2.: Fitting and extrapolation of thermal conductivity at 300K for CsF without lattice expansion.



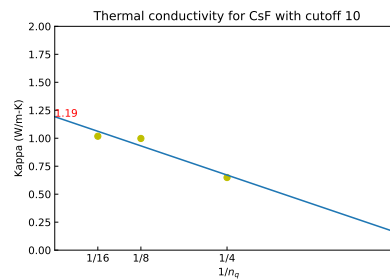
(a) Thermal conductivity for CsF with cutoff distance 2.5 Å.



(b) Thermal conductivity for CsF with cutoff distance 5 Å.



(c) Thermal conductivity for CsF with cutoff distance 8 Å.



(d) Thermal conductivity for CsF with cutoff distance 10 Å.

Figure B.3.: Fitting and extrapolation of thermal conductivity at 300K for CsF with lattice expansion.

C. Vibrational properties of Strongly Anharmonic LiGaTe

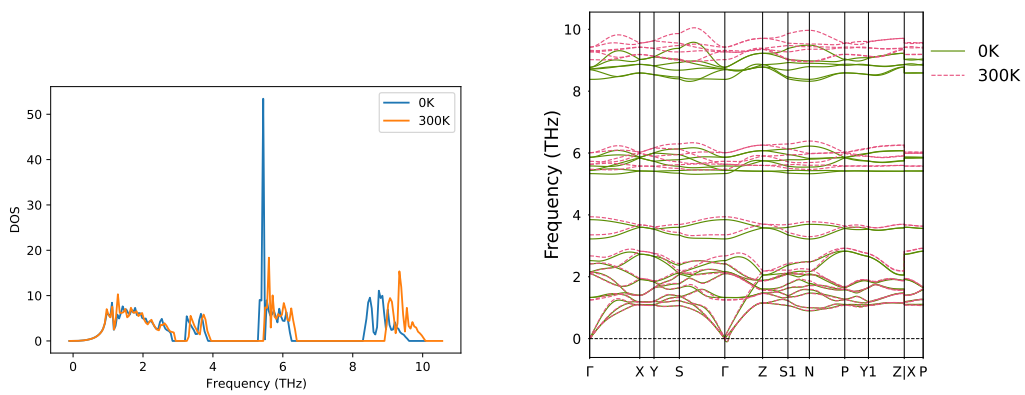


Figure C.1.: Phonon band structure and DOS for LiGaTe

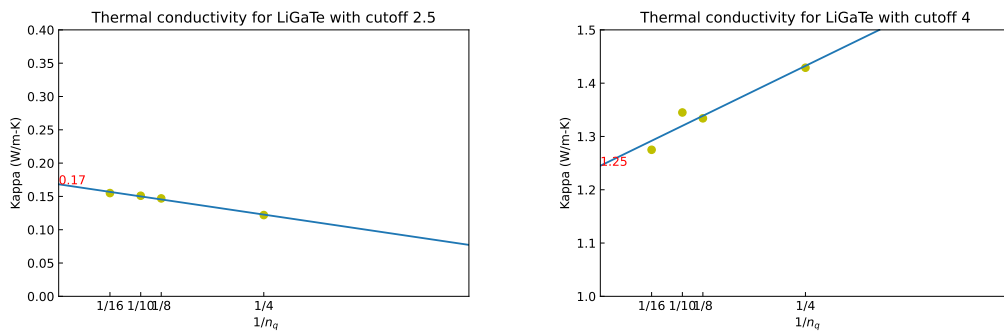


Figure C.2.: Fitting and extrapolation of thermal conductivity at 300K for LiGaTe with lattice expansion

D. Vibrational properties of Strongly Anharmonic LiI

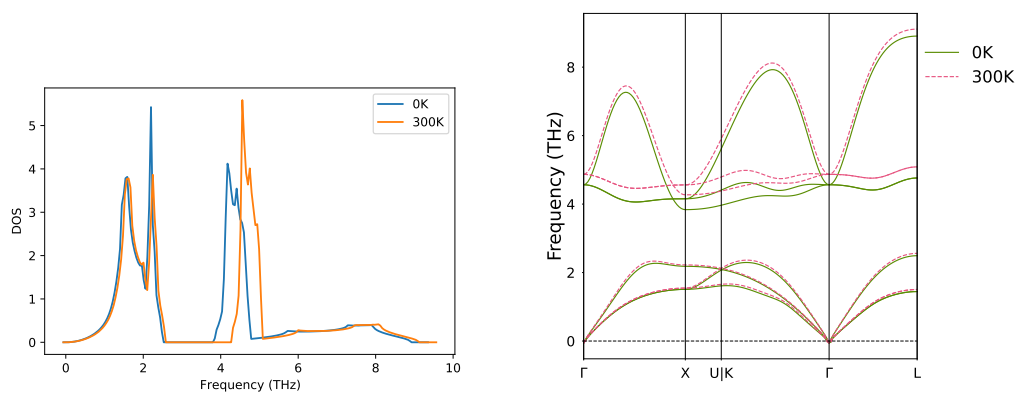
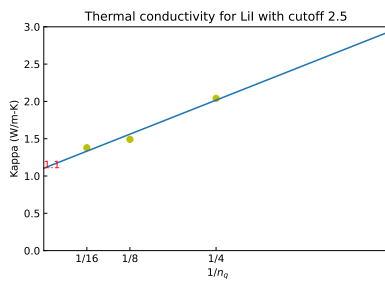
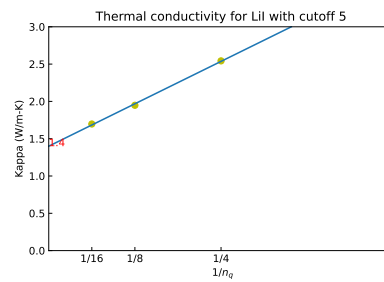


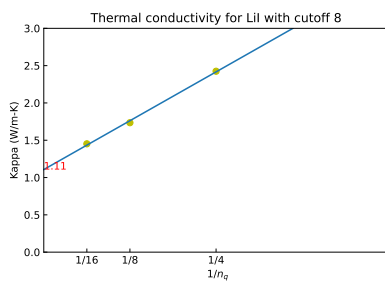
Figure D.1.: Phonon band structure and DOS for LiI.



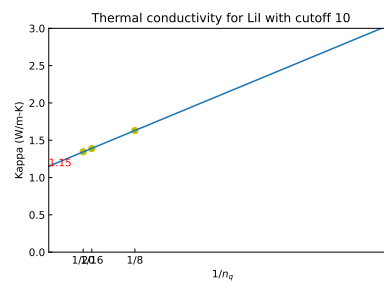
(a) Thermal conductivity for LiI with cutoff distance 2.5 Å.



(b) Thermal conductivity for LiI with cutoff distance 5 Å.

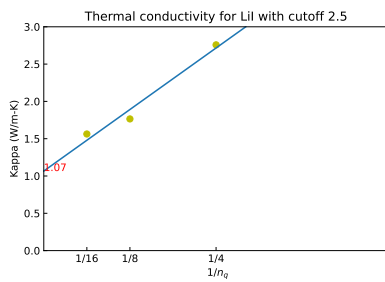


(c) Thermal conductivity for LiI with cutoff distance 8 Å.

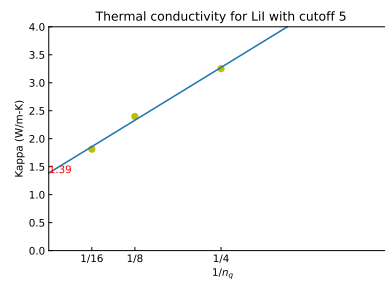


(d) Thermal conductivity for LiI with cutoff distance 10 Å.

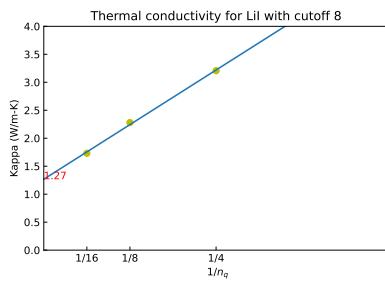
Figure D.2.: Fitting and extrapolation of thermal conductivity at 300K for LiI without lattice expansion.



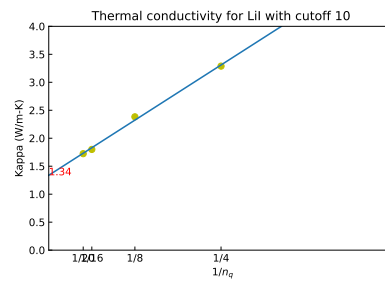
(a) Thermal conductivity for LiI with cutoff distance 2.5 Å.



(b) Thermal conductivity for LiI with cutoff distance 5 Å.



(c) Thermal conductivity for LiI with cutoff distance 8 Å.



(d) Thermal conductivity for LiI with cutoff distance 10 Å.

Figure D.3.: Fitting and extrapolation of thermal conductivity at 300K for LiI with lattice expansion.

E. Vibrational properties of Strongly Anharmonic KCaF

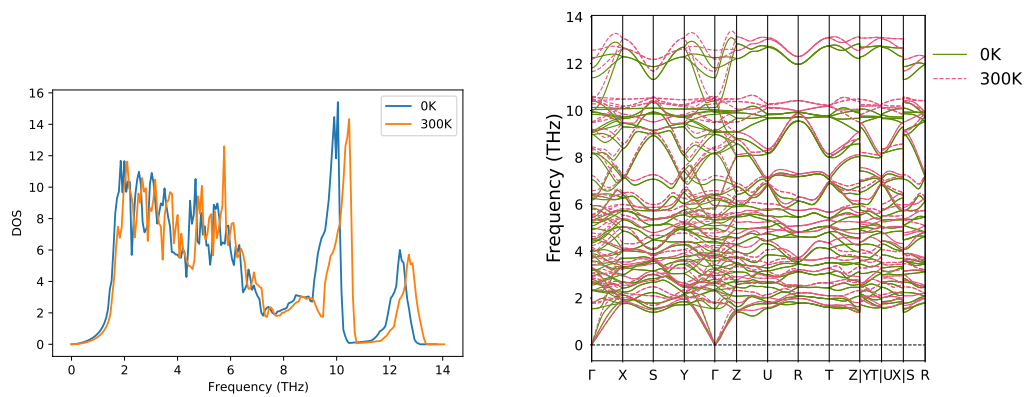
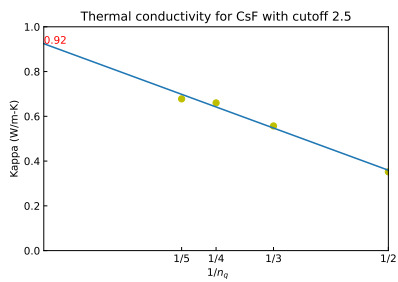
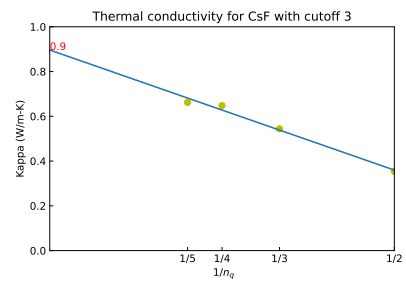


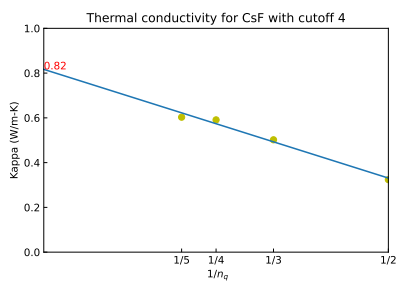
Figure E.1.: Phonon band structure and DOS for KCaF



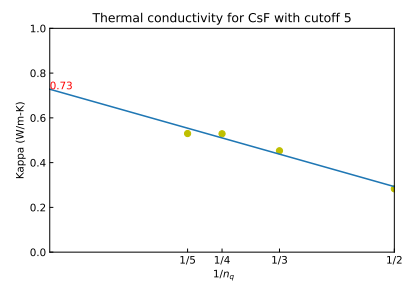
(a) Thermal conductivity for KCaF with cutoff distance 2.5 Å.



(b) Thermal conductivity for KCaF with cutoff distance 3 Å.

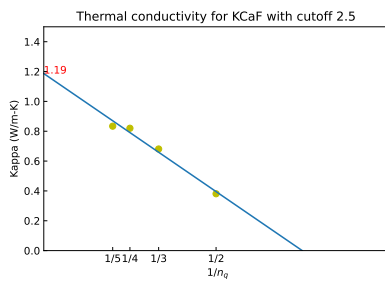


(c) Thermal conductivity for KCaF with cutoff distance 4 Å.

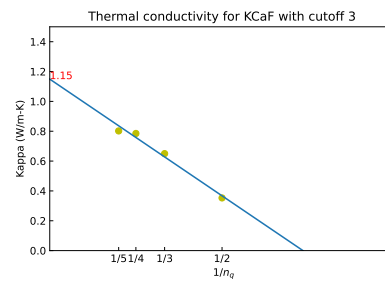


(d) Thermal conductivity for KCaF with cutoff distance 5 Å.

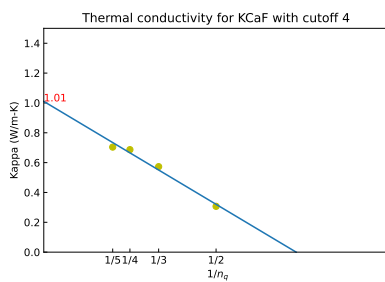
Figure E.2.: Fitting and extrapolation of thermal conductivity at 300K for KCaF without lattice expansion.



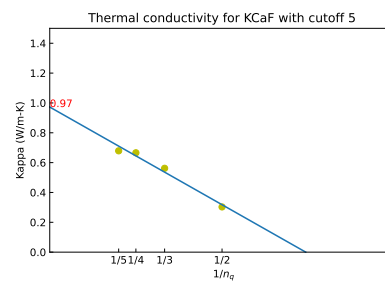
(a) Thermal conductivity for KCaF with cutoff distance 2.5 Å.



(b) Thermal conductivity for KCaF with cutoff distance 3 Å.



(c) Thermal conductivity for KCaF with cutoff distance 4 Å.



(d) Thermal conductivity for KCaF with cutoff distance 5 Å.

Figure E.3.: Fitting and extrapolation of thermal conductivity at 300K for KCaF with lattice expansion.